Society for Science and Education
United Kingdom

ISSN: 2055 - 1266
Volume 4 No 5
Oct 2017

Journal of Biomedical Engineering and Medical Imaging

TABLE OF CONTENTS

EDITORIAL ADVISORY BOARD

DISCLAIMER

All the contributions are published in good faith and intentions to promote and encourage research activities around the globe. The contributions are property of their respective authors/owners and the journal is not responsible for any content that hurts someone's views or feelings etc.

Society for Science and Education United Kingdom

JBEMi JOURNAL OF BIOMEDICAL ENGINEERING AND MEDICAL IMAGING

ISSN: 2055-1266
Volume 4 Issue 5

Monitoring System of Mechanical Activity of the Heart and Goelocalization of the Patient Based on the Mqtt Cloud

[1]André R. Tchamda, [2]R. Tchitnga, [3]Francois. B. Pelap, and [4]M. Kom
[1, 2] *Physics Department electronic option, University of Dschang, Dschang , Cameroon;*
[3] *Physics Department mechanical option, University of Dschang, Dschang , Cameroon;*
[4] *Department of Electrical Engineering and Telecommunication, University of Yaounde I, Cameroon*
andre.tchamda@eaphysud.org; robert.tchitnga@eaphysud.org; fbpelap@yahoo.fr;
kommart@yahoo.com

ABSTRACT

The queue of patients for consultation and appointments that we observe in our health centers is growing in size from day to day given the exponential growth of the human population. Medical systems based on telemonitoring have been developed to remotely monitor the health status of patients. In this work, we constructed a medical prototype for remote monitoring of the mechanical activity of the heart and for geolacalization of the patient based on Message Queue Telemetry Transport (MQTT). The prototype will be used by individuals or by health centers without a doctor. The geolacalization will enable us to locate the injured individual. The physiological data and GPS coordinates are collected using a portable kit and are transmitted directly to an MQTT cloud using a Wi-Fi hotspot. A web server hosted in the kit allows the user to enter the service set identifier (SSID) of the access point through a smartphone. MQTT cloud will take care of the storage, geolacalization and transmission of the signal from the mechanical activity of the heart to the doctors. Almost all smart terminals with a web browser can easily access data (smartphone, tablet, computer). Tests carried out on individuals reveal that the proposed prototype is reliable in sampling, real-time transmission and geolacalization in street map and imagery, which can help in diagnosis and rapid intervention.

Keywords: heart activity; telemonitoring; MQTT Cloud; internet; geolacalization.

1 Introduction

OASIS, (Organization for the Advancement of Structured Information Standards), a global consortium working on the standardization of open file formats based on XML, has just announced that it has chosen the Message Queuing Telemetry Transport (MQTT) as the message protocol for Internet of the Objects, opening the doors to a market of several million dollars. "Today, one of the big challenges is that there is no clear open standard to enable embedded systems to communicate with each other," said Mike Riegel, vice president of marketing, Mobile Solutions Group IBM. Historically, we know that if we do not have an open standard like this, it is not possible to make the necessary progress", he added. "Just as the HTTP standard has paved the way for information exchange on the web, the MQTT could set the stage for bringing billions of low-cost telemetry terminals online to collect embedded data," Said the

DOI: 10.14738/jbemi.45.3679
Publication Date: 2nd October, 2017
URL: http://dx.doi.org/10.14738/jbemi. 45.3679

vice president of IBM [1]. The GSM Association (GSMA) estimates that by 2020, 15 billion terminals of this type will be put online. And Cisco believes that this market could represent more than $ 14 billion in sales for IT providers.

MQTT is an open protocol, simple, lightweight and easy to implement. This protocol is ideal to respond to the following needs: Particularly adapted to use a very low bandwidth, Ideal for use on wireless networks, Low power consumption, Very fast, it allows a response time superior to other present standards of the web. Provides high reliability if needed, requires few processor and memory resources. MQTT is a simple and lightweight TCP / IP messaging service. Messages are sent by publishers on a Topic to a broker. These messages can be read by subscribers. Topics can have a hierarchy that allows you to fine-tune the information you want. In the MQTT protocol, exchanges are secured at several levels: Transport and Authentication.

MQTT is a publication/subscription (Pub / Sub) messaging protocol that is particularly well suited to work in an environment with limited computing power and minimal network connectivity. IBM and the supplier of Eurotech systems developed the MQTT before contributing to Oasis. The protocol is already used in a wide variety of embedded systems. For example, oil and gas companies use the MQTT to monitor thousands of kilometers of pipelines. Large livestock farms, large farm structures use this protocol. Today, almost all the physical objects we see (appliances, appliances, etc.) are also connected to the MQTT. To strengthen the MQTT, Oasis has set up a new technical committee. Its objective: to ensure that the MQTT is able to work with other types of networks, devices and software applications. The engineers from Cisco, IBM, Red Hat, Software AG and Tibco, and others will support the project.

The financing of medical care has become the most important point these days and the most costly for governments. Health and medical care can also benefit fully from the deployment of MQTTs for remote diagnosis, remote health surveillance and care for the elderly [2]. MQTT should reduce patients' consultation and transportation costs. It will also bring physicians closer to some patients who live in the isolated areas without health centers. This MQTT protocol can also be used to geolocate patients requiring rapid intervention and are not able to issue an alarm signal. This is one of the points we have developed in this work. In this work, we constructed a prototype based on MQTT to monitor the mechanical activity of the heart. The prototype can also take into account the measurement of the electrical activity of the heart by just replacing the sensor module. The prototype is equipped with a microcontroller integrated circuit with Wi-Fi connection called EPS-12E. This circuit will first connect to a Wi-Fi access point, secondly will take care of recovering signals and transmitting them on the MQTT canvas for viewing by the doctor. The integrated circuit will also retrieve the geolocalization coordinates and transmit it on the MQTT canvas for a patient localization. This prototype with a powerful 80 MHz processor has the advantage of being portable and equipped with a web server hosted in the EPS-12E circuit which permits entering of the identifier of an access point, this enables the use of the module anywhere in the world as long as Internet connection is available. The web server integrated in the circuit offers a possibility of visualization of the collected signals, which will make it possible to use the prototype within a radius of 0-200m without needing to connect to the internet. The data is stored in the Cloud MQTT server and can be exported as CSV file, allowing researchers and students to access the signal for application of the course on signal processing.

Therefore, the system proposed in this work reveals a unique design and management compared to previous works [3-10], including the use of ESP-12E as a Web server for viewing data in a locality where an internet connection does not exist in the distance between patient and doctor. Some existing devices are limited in transmission distance, which prevents the patient from performing activities around the world [4, 11-12]. In addition, medical devices are generally very expensive devices for personal use, patients must regularly visit health centers, which will inevitably increase the burden on these centers. In order to overcome the problems illustrated above, we have built a low-cost, short-range, high-cost portable prototype with geolocalization that can be connected to all smart terminals with a web browser.

The rest of the work will be presented as follows. The section "Architecture of the monitoring system mechanical activity based on the MQTT", followed by the section "Prototype of acquisition of the mechanical activity of the heart", followed by the section "Experimental results" which we perform on a volunteer in Good health to verify the reliability of the proposed prototype, and finally the conclusion section.

2 Architecture of Monitoring System Mechanical Activity Based on MQTT

This architecture presented in figure 1, which mainly consists of three parts as follows: device for detecting the mechanical activity of the heart, MQTT cloud and the doctor's interface.

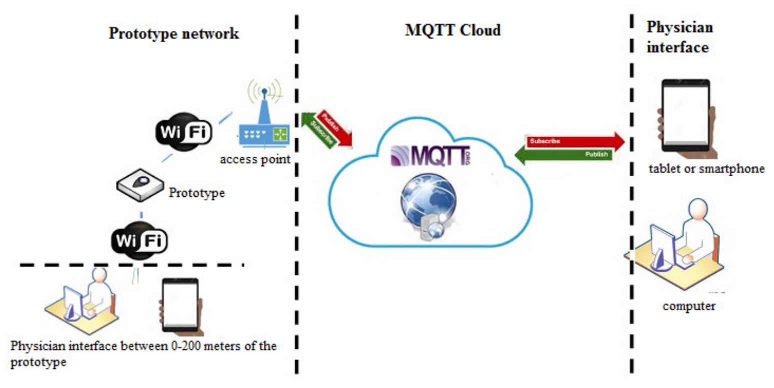

Figure 1: Architecture of the monitoring system.

2.1 Device for Detecting the Mechanical Activity of the Heart

This device is the departure of the entire prototype, which is responsible for the collection and transmission of physiological signals from the patient to the MQTT Cloud via a wireless Wi-Fi link. The signals will be recovered by a sensor, and will undergo amplification, filtering and conditioning before being processed by the microcontroller. The data collected by the sensor are transmitted to the MQTT cloud via the wireless Wi-Fi protocol. A GPS module is used to have the patient's coordinates, which will help to locate him for an intervention in case of danger. This protocol provides a sufficient data transfer rate for the transmission of our physiological data.

A web server is hosted in this device and plays two roles:

- **First role:** An SSID (Service Set Identifier) is a 32-character alphanumeric key that uniquely identifies a wireless network. Its purpose is to prevent other wireless equipment from accessing your local network, either accidentally or intentionally. The local network also has a password.

In order for the device to connect to any access point, a web interface is provided to enter the SSID and the password of this access point.

- **Second role:** if the patient is close to the doctor, say a radius of 0-200 meters, there is no need using the internet for data transfer. Since the patient is close, another web interface housed in the device makes it possible to visualize the patient's signal. A signal taken from a normal person over two meters is shown in figure 5.

A smartphone, a tablet or a computer can be used to connect directly to the microcontroller's Wi-Fi (ESP-12E) to perform the first and second roles.

2.2 MQTT Cloud

This central part of our architecture for monitoring the mechanical activity of the heart. The MQTT cloud is used retrieve the data collected from the patient and to transmit the data to the doctor's interface. MQTT cloud consists of a data storage module, which is very important for subsequent analysis of the signal. It will also be able to export patients' data as a file (XML, JSON, CSV), which may help students and researchers during the application of signal processing. After having retrieved the coordinates coming from the GPS module, the MQTT Cloud will take care of making a geolacalization in street map and satellite imagery.

2.3 Doctor's Interface

This interface is accessible from all platforms using an operation system and a browser, for example: smartphone, tablet and computer. The interface provides easy access to data in the MQTT Cloud. The doctor logs in to the cloud to export the data, view the data and the patient's geographic location. The geographical location is visible on the doctor's interface in street map and satellite imagery mode, this will allow the doctor to immediately follow the patient's current location and send him an ambulance. The use of tablets and smartphones allows a great mobility of the doctor.

3 Prototype for Acquisition of Mechanical Activity of the Heart

The design of our prototype is presented in figure 2 and consists of: Sensor module, Controller / Wi-Fi module, GPS module, Power module.

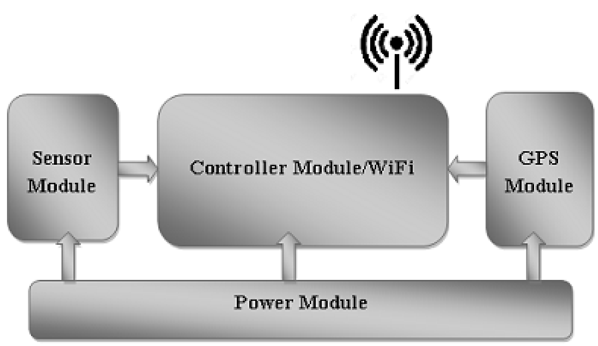

Figure 2: Components of the prototype

The architecture proposed by our prototype is less cumbersome and less expensive compared to the existing ones. Existing prototypes need an additional Bluetooth module to connect to a smartphone that transfers data to the cloud [12-13]. Other existing prototypes do not allow a geolocalization of the patient [12-15]. Figure 3 shows the physical prototype. It will be detailed as follows.

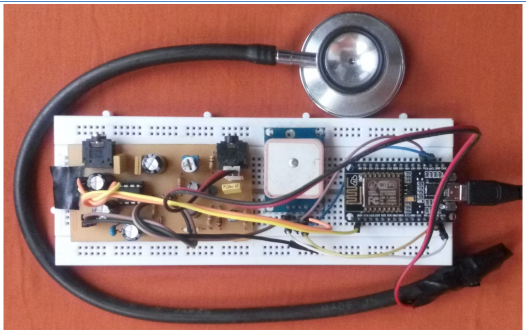

Figure 3: Physical prototype

3.1 Sensor Module

The module includes a Panasonic's WM-63PRT microphone used to pick up the sound produced by the mechanical movement of the heart. This microphone has an excellent frequency response with amplitude of 10-20 mV and a frequency of 20 Hz to 16 kHz [16]. The module consists of an amplifier to amplify the microphone signal followed by a Band-pass filter of 10-500Hz. A Band-pass filter is used to eliminate noise outside this frequency band. Finally, using the controller module, signals are collected

3.2 Controller / Wi-Fi Module

Controller / WI-FI module used here is ESP-12E. The ESP-12E is a low-cost Wi-Fi chip with full TCP / IP stack and MCU (microcontroller unit) capability. It is used to recover the signal at the sensor module output and send it to its built-in Wi-Fi module. This MCU is widely used in web applications, because of its Wi-Fi that supports Wi-Fi (802.11b/g/n). The microcontroller includes 32-bit RISC CPU running at 80 MHz, a flash memory up to 4 Mbyte and 96 Kbyte of RAM. The MCU also provides other functions such as analog to digital converter (ADC), Pulse Width Modulation (PWM), Serial Peripheral Interface Bus (SPI) and universal asynchronous receiver / transmitter (UART).

The microcontroller will sample the analog signal at the output of the sensor module. According to Shannon's theorem, the sampling frequency is set to 1 KHz, given that the measured signal is generally between 10 Hz and 500 Hz.

The higher the sampling frequency, the better the reproduction of the start signal, which will cause no problem if the sensor module is replaced by another module used to measure another physiological signal and as long as the maximum value of the this signal will be less than 500HZ. In order to respect this sampling time, we have fixed a TIMER interrupt which will take place every 1/1000 seconds. The scanned data is transmitted internally to the Wi-Fi module integrated in the MCU and then routed to the Wi-Fi access point.

3.3 GPS Module

The GPS module used here is GY-NEO6MV2. Printed circuit boards with the indication GY-NEO6MV2 are very popular and cheap on the internet. NMEA messages are available, with a standard speed of 9600 bits / sec, at the TX output of the printed circuit board. To communicate with microcontrollers, it has a UART port. Queried by the MCU, it returns the longitude, latitude and altitude of the patient's position. This information will be sent to the MQTT broker.

3.4 Power Module

The power module provides a reliable power supply to each module of our device. The power supply is via the USB port or a lithium battery.

4 Where to Capture the Sounds Produced by the Mechanism of the Heart

The words reserved for this are cardiac auscultation. The noises of the heart beats are mainly noises of fluids (blood) and materials (valves), more precisely: dynamic events, Contraction and relaxation of the atria and ventricles, the movement of valves. The blood flow, the turbulence of the blood at the time of closing of the valves.

The auscultation of the heart is mainly concerned with listening to these noises that occur inside the body via a stethoscope. The optimal auscultation sites (figure 4) are:

- ***Mitral focus***: The blood passing through the mitral muscle is directed towards the tip of the heart. The best perception is at the level of the 5th intercostal space, on the mid-clavicular line, in sub-mammary position.
- ***Tricuspid focus***: as the heart is lying at 45 °, the blood flow through the tricuspid valve goes downwards: the tricuspid is best heard at the xiphoid focus.
- ***Aortic focus***: the inner end of the second right intercostal space, corresponding to the main auscultation focus of the aortic sigmoid.
- ***Pulmonary focus***: the inner end of the second left intercostal space, along the sternum, corresponding to the pulmonary sigmoid valves, incidentally to the aortic valves (accessory aortic focus extending along the left margin of the sternum).

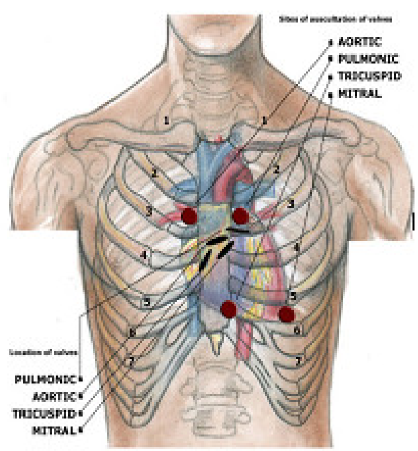

Figure 4: Cardiac Auscultation Foyers

5 Display of Experimental Signals

To verify the reliability of our prototyping, experiments were conducted on normal people. The prototype offers an option to view a patient's data without having to go through the cloud MQTT. This is useful when the doctor is close to the patient. An HTTP server hosted in the device can display the patient's signal on a browser. From JavaScript, the canvas element was used to create the signal. Figure 5 shows the display of the signal over a very short distance between doctor and patient

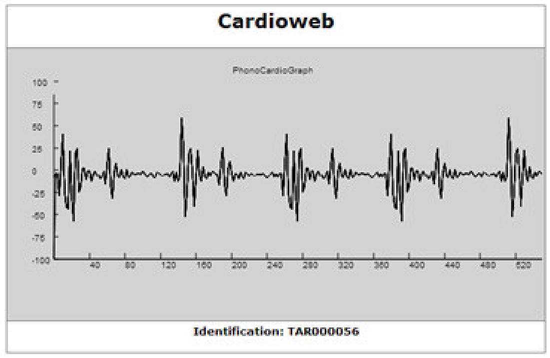

Figure 5: Example of visualization by integrated web server

Figure 6 shows the reception of the data via the MQTT. It shows us the reception of a signal describing the mechanical activity of the heart. We will also notice two images to the right of the curve. These images are images showing the geolocalization of the patient in two modes (street map, satellite imagery). The blue dot on these images marks the position of the patient. An error margin with respect to this point of 8.5 meters must be taken into account.

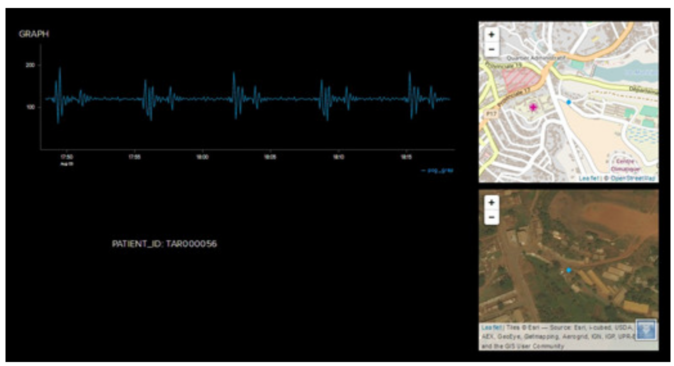

Figure 6: Example of geolocation and visualization of the mechanical activity of the core by MQTT cloud

6 Conclusion

We put in place a prototype for monitoring the mechanical activity of the heart based on a state-of-the-art technique called the MQTT. The architecture of the surveillance prototype was presented. Typical networks for detecting the mechanical activity of the heart were introduced and compared. With the portable monitoring device containing a high-sensitivity microphone, real-time signals can be collected with satisfactory accuracy. The data collected was transmitted to the MQTT Cloud using Wi-Fi, which supports high data transfer rates and large coverage areas. MQTT Cloud is responsible for storing data and permitting doctors to view the signal. MQTT is also responsible for carrying out a geolocalization and to display it on the doctor's interface. Such a prototype can be used by hospitals and even by individuals due the fact that it is very potable and less costly.

REFERENCES

[1] Lemondeinformatique., *http://www.lemondeinformatique.fr/actualites/lire-mqtt-futur-protocole-de-l-internet-des-objets-53422.html,* 2017 .

[2] Islam, S.M.R., et al., *Internet of Things for health care: a comprehensive survey*. IEEE Access, 2015. 3.

[3] Lars-Jochen, T., G. Colicchia and R. Girwidz, *Phonocardiography with a smartphone*. Phys. Educ. 2017. 52.

[4] Abdel-Motaleb, I.M., and V. K. Sambaraju, *Development of a Wireless Cardiogram System for Acute and Long-term Healthcare Monitoring*. EIT Conf, 2012.

[5] **Mbiadoun, T., M. kom and P. N.Eloundou**, *Universal Module of Acquisition and Transmission of Electrophysiological Signal*. IJIRSET, 2014. 3: p. 13767- 13776

[6] Jusak and I. Puspasari, *Wireless tele-auscultation for phonocardiograph signal recording through the zigbee networks*, IEEE Asia Pacific Conference on Wireless and Mobile (APWiMob), 2015.

[7] Sa-ngasoongsong, A., et al., *A low-cost, portable, high-throughput wireless sensor system for phonocardiography applications*. Journal of Sensors, 2012. 12: p. 10851-10870.

[8] Tchamda, A. R., et al., *Low-Cost Phonocardiogram Board with Graphic LCD, Solar Panel and Embedded Heart Sound Analyser*, IJIRSET, 2015. 4: p. 18793- 18799.

[9] Junaid M., et al., Internet of Things: Remote Patient Monitoring Using Web Services and Cloud Computing, Cyber-Physical-Social Computing, 2014.

[10] Zhao, Z, and Shengkang He, *A Heart Sound Transmission and Reception System Based on NFC and Bluetooth*, IFMBE Proceedings, 2014. 42: p. 187- 190.

[11] Chien, J. C, and C-C Tai; *A New Wireless-Type Physiological Signal Measuring System Using a PDA and the Bluetooth Technology*, Proceedings of the 2006 IEEE International Conference on Industrial Technology, 2006: p. 3026-3031.

[12] Amiri, A. M., K. Mankodiya, and G. Armano, *PhonoSys: Mobile Phonocardiography Diagnostic System for Newborns*, ICST , 2015.

[13] Hassanalieragh, M., et al., *Health Monitoring and Management Using Internet-of-Things (IoT) Sensing with Cloud-based Processing: Opportunities and Challenges*, IEEE computer society, 2015.

[14] Uttam U. D., and M. A. Kulkarni, *IoT based Real Time ECG Monitoring System using Cypress WICED*, ijareeie, 2017. 6(2).

[15] Savita, F., and S. Vashist, *Design and Implementation of Wireless Body Area Network using Physiological Parameters*, JOURNAL OF BIOMEDICAL ENGINEERING AND MEDICAL IMAGING, 2017. 4(1): p. 13-20.

[16] Van Rhijn, A., *Integrated Circuits for High Performance Electret Microphones*, Audio Engineering Society AES-E-Library the 114th conference, 2003: p. 5719.

SOCIETY FOR SCIENCE AND EDUCATION
UNITED KINGDOM

JBEMi JOURNAL OF BIOMEDICAL ENGINEERING AND MEDICAL IMAGING

ISSN: 2055-1266
VOLUME 4 ISSUE 5

A Effectual Technique of Impulse Noise Suppression for Assessing the Impact of Brain Disorders in MRI by applying Selective Weighted Median Filter

[1]Sudheesh.K.V, [2]Dr.L.Basavaraj

[1]*Research Scholar, Department of Electronics and Communication Engineering, ATME College of Engineering, Mysuru, Karnataka, India*

[2]*Professor, Department of Electronics and Communication Engineering, ATME College of Engineering, Mysuru, Karnataka, India*

sudheesh.vvce@gmail.com; basavaraj.atme@gmail.com

ABSTRACT

An accurate analysis of medical images is progressively demanding in providing the absolute detection and diagnosis of diseases in medical imaging. The significant pre-processing step in MRI data processing is noise elimination. Noise deletion is essential step to increase image quality and performance of all the tasks desirable for quantitative imaging analysis. In this paper a new scheme for impulse noise removal in corrupted MRI brain images is introduced. The proposed scheme is a simple & efficient filtering technique that effectively detects and removes the salt and pepper noise. The experimental results of suggested noise purifying process executed on standard set of assessment images shows that algorithm provides a very good results with low mean-squared-error and high signal-to-noise ratio values for noise density up to 95% and outperforms significant tradeoff between fine detail preservation and noise removal in brain MRI images.

Keywords: Selective weights, Denoising, Salt and pepper noise.

1 Introduction

In recent days, the technology of computer is extensively used in the arena of medicine. The significant area of interdisciplinary exploration is interpreting and analyzing the medical images. Many types of imaging techniques are employed for diagnosing the brain disorders in patients non-invasively without any human involvement. MRI (Magnetic Resonance Imaging) is one such advanced imaging technology which plays a vital role in creating a high quality images of human body parts, specially the parts of human brain. In image processing the two most common types of noise are Gaussian noise and Impulse noise also called as salt and pepper noise. The impulse noise in digital image is caused by malfunctioning pixels in camera sensors, defective memory cells in hardware unit or due to image transmission in noisy channel [9]. Specially, brain MRI images are more sensitive to one typical practice of impulse noise called as salt and pepper noise. Salt and pepper noise through same likelihood disturbs the quality of image by randomly corrupting the

DOI: 10.14738/jbemi.45.3686
Publication Date: 10th October, 2017
URL: http://dx.doi.org/10.14738/jbemi. 45.3686

pixels with two extreme values 0 (black) and 255 (white) also it degrades the finest details in the medical image such as edges, textures and contours. These noises in the medical images are inevitable but removal of those noises are mandatory to boost the visual excellence of image. Thus the work focuses on exclusion of impulse noises present in the brain MRI images to realm the reliability of finest element features associated with images. Thus, in this regard the paper highly proposes the new median filtering approach based on selective weights of filter for removal of impulse noises. The performance of the denoising algorithm are evaluated using statistical noise parameters such as SNR, PSNR and MSE. The results shows that the proposed method reconstructs the high quality image to have a superior performance even at very noise density values.

2 A new enhanced Median Filtering Approach

Even though there are several filters available for impulse noise reduction, certain filters are best suited for some particular class of images (brain MRI Images). In most of the prevailing algorithms which includes Standard Median Filter and Center Weighted Median Filter, merely median values are used for the replacement of the degraded pixels. Therefore, in proposed algorithm we have designed improved method noise removal filter based on the statistical parameters approach in order to restore the actual input image from the degraded image. Thus, the procedure involves mainly two phases. In first phase of process, the detection of noisy pixels which is standard responsible for degradation of image is performed. The second step of process involves removal of noisy pixels and replacing those noisy pixels with noise free pixels by applying the proposed noise filtering technique. Figure 1 shows the depiction of brain MRI noisy image. In this work T2 weighted real time MRI images are used. T2 weighted images have better contrast to detect soft tissue related abnormalities which helps in classification of brain MRI images. The two sets of MRI images are collected from pathology labs a) normal images and b) abnormal images i.e. images with different abnormalities. The evaluation of proposed approach involves the T2 weighted MRI images are acquired by short echo time from Intera Philips 1.5 Tesla MRI scanner. The scanner produces the images 5mm slice thickness whose resolution varies from 256X256 to 958X958. One of the T2 weighted brain MRI image (normal and abnormal) considered in the database is shown in Figure 1.

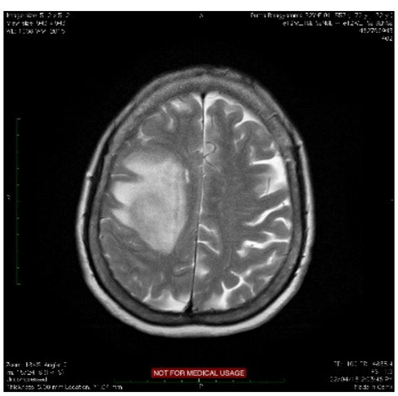

(Abnormal Image)

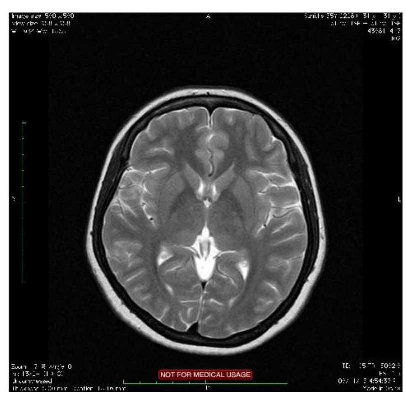

(Normal Image)

Figure 1 Original Abnormal and Normal brain MRI images

2.1 Noise Detection

The most common noise present in brain MRI images is Impulse noise likewise called salt and pepper noise. A brain MRI image containing impulse noise consists of darker pixels in brighter sections and brighter pixels in darker sections. The impulse noise with same probability disturbs the quality of the image by randomly corrupting the pixels with two extreme values 0 (black) and 255 (white). The detection of impulse noise in brain MRI image can performed based on its probability density function (PDF). The PDF helps in describing the nature of the salt noise and pepper noise according to equation 1.

$$p(k) = \begin{cases} P_z & for\, k = z \\ P_y & for\, k = y \\ 0 & otherwise \end{cases} \tag{1}$$

Given the probability p(k) ranging from 0 to 1 for that a pixel degraded, the salt and pepper noise can remain observed in an image by making probability equal to 0.5p(z) by randomly selected pixels to white (salt noise) and remaining probability of 0.5p(z) by randomly selected pixels to black (pepper noise).

The method for determining salt and pepper noise is also performed using morphological approach called as open close residue factors. Here, the corrupted pixels from either salt noise or pepper noise are detected by open and close residue operators. The open operator in the morphological function is responsible for determining the salty pixel and close operator is responsible for determining the pixel corrupted from pepper noise. The open and close operations on noise pixels is performed by equation 2 and 3.

$$\mathrm{R_o}\ (\mathrm{i, j}) = \mathrm{f} - \mathrm{f} \circ \mathrm{b} \tag{2}$$

$$\mathrm{R}_c (\mathrm{i, j}) = \mathrm{f} \bullet \mathrm{b} - \mathrm{f} \tag{3}$$

The corrupted pixels can be determined through equating equation 2 and equation 3 with threshold T as well-defined in equation 4.

$$s(i, j) = \begin{Bmatrix} 1, R_o(i, j) \geq T \\ -1, R_c(i, j) \geq T \\ 0, Otherwise \end{Bmatrix} \tag{4}$$

Here, if $s(i, j)$ = 1, then $R_o(i, j)$ is determined as salt noise and if $s(i, j)$ = - 1, then $R_o(i, j)$ is determined as pepper noise. If $s(i, j)$ = 0, then $R_o(i, j)$ is taken as noise less pixel.

2.2 Noise Removal Technique

The work proposes a novel filtering approach called as Selective Weighted Median filter which is most effective over the Impulse (Salt and Pepper) noise commonly present within brain MRI images. The proposed filter method is variant of weighted and center weighted median filter which not solitarily considers rank command statistics nevertheless also deliberates spatial data. This filter preserves the image details by removing the additive white noise or impulse noise. It is special because of its perfectness and simplicity which means that the design of the filter is easy and the theory behind it can be easily understood. The elementary knowledge is to assign larger weights to the center pixel and the remaining pixels are assigned 1 in each window. The operation is same as median filter but the weights contains varying weights which is multiplied with original image pixels. The following shows the algorithm steps of the proposed filtering process.

2.2.1 Selective Weighted Median Filtering Algorithm

In the proposed selective weighted median filter, all the coefficients of the filter mask will have random values.

1. Consider a 3X3 mask such that highest weightage is assigned to the center pixel.
2. Next highest weightage is assigned to the four neighbors pixels of that center pixel.
3. Least weightage is assigned to the four diagonal neighbors of that center pixel.

1	1	1
1	8	1
1	1	1

(Step 1)

1	4	1
4	8	4
1	4	1

(Step 2)

1	4	1
4	8	4
1	4	1

(Step 3)

4. Apply the 3X3 filter mask at the leftward angle of the noisy image.
5. Multiply the filter mask with the pixel value of the input noisy image.
6. After subsequent multiplication, along with center pixel arrange all four neighboring pixels of that center pixel in ascending or descending order.
7. Select the median from these five values.
8. Similarly, along with center pixel arrange all four diagonal neighboring pixels of that center pixel in ascending or descending order.
9. Select the median from these five values.
10. Replace the average of two median values at the center and move the mask throughout the noisy image and repeat the steps.

3 Image Statistical Criteria

The performance of the denoising algorithms are evaluated using statistical noise parameters. The statistical evaluation criteria of noises in image is used to measure the degree of improvement of the image. In this analysis the concert of every filter is calculated quantitatively for brain MRI image with impulse noise via following image evaluation criteria in directive to investigate the competence of filtering algorithms. The image statistical evaluation criteria are Signal to Noise Ratio (SNR), Peak Signal to Noise Ratio (PSNR), Structural Similarity Index (SSI), and Mean Squared Error (MSE).

3.1 SNR Estimation

SNR is physical degree of sensitivity of image. Larger the SNR values represents that the quality of the filtered image is noble and it is given by

$$SNR = 10\log_{10}\frac{\sum_{l=1}^{P}\sum_{k=1}^{Q}(f(l,k)^2 + g(l,k)^2)}{\sum_{l=1}^{P}\sum_{k=1}^{Q}(f(l,k)^2 - g(l,k)^2)} \qquad (5)$$

Where, *f(l, m)* is original image and *g(l, m)* is filtered image.

3.2 PSNR Estimation

PSNR is utmost regularly used as measure of excellence of denoised image. Greater PSNR rate designates that filtered image is of greater quality with less amount of noise. It is defined as

$$PSNR = 10Log_{10}(\frac{Max^2}{MSE}) \qquad (6)$$

Where, MAX^2 is the maximum intensity in the denoised images.

3.3 SSI Estimation

SSI is used in lieu of gaging the resemblance between output image and input image. If the enactment of filter stands effectual in eliminating impulse noises then SSI must be less than 1 and it is given by

$$SSI = \frac{\sqrt{Var(g(l,k))}}{Mean(g(l,k))} X \frac{Mean(f(l,k))}{\sqrt{Var(f(l,k))}} \qquad (7)$$

3.4 MSE Estimation

MSE for two images [28] where one of the images is reflected as noisy estimate of the other is defined as

$$MSE = \frac{1}{PQ}\sum_{l=1}^{P}\sum_{k=1}^{Q}(f(l,k) - g(l,k)) \qquad (8)$$

4 Experimental and Outcomes

Gray-scale images of size 560×560 have been used to test the performance of the algorithm with dynamic range of values (0, 255). The different noise removal algorithms are tested and simulated. Denoising process is carried out for brain MRI images using the different standard impulse lessening filters such as Standard Median mesh (filter), Adaptive Median mesh, Center Weighted Median mesh, and proposed filtering approach called as Selective Weighted Median filter.

The image produced by the MRI scanners appears to be gray scale images but some images contains color bar and other details like markings and labels which are represented with different colors. Therefore it is necessary to ensure that the images are converted gray scale so that different image processing operations can be performed and the analysis becomes easier. In RGB image the corresponding intensities of red, green and blue values are the constituents of a pixel. By keeping the luminance unchanged and eliminating hue and saturation gray scale conversion is attained by

$$g = \left(\frac{3}{10}\right)R + \left(\frac{29}{50}\right)G + \left(\frac{11}{100}\right)B \tag{9}$$

The Original image is as shown in Figure 2, and the image subjected to impulse noise (noisy image) before and after grayscale conversion is as shown in Figure 3 and Figure 4 respectively.

Figure 2 Original Brain MRI image

Figure 3. Noisy Image

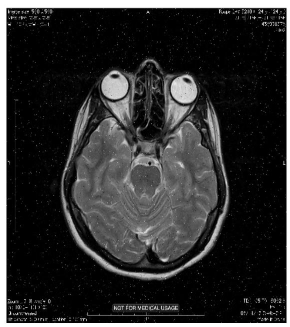

Figure 4 Noisy Image with Grayscale converted

Images will be corrupted by salt-and-pepper noise at different noise levels such as low noise level (30%), medium noise level (60%) and high noise level (95%). Then the proposed filtering technique is applied to the corrupted image to remove the noise, yielding the restored gray-scale image. The denoised Image (after grayscale conversion) at different noise levels obtained after applying standard median filter, adaptive weighted median filter, and center weighted median filter and proposed selective weighted median filter for the considered example is as shown in Figure 5. The experimental tables I, II, III in this section indicates the comparative analysis of performances of different denoising median filtering algorithms at different noise levels such as low noise level (30%), medium noise level (60%) and high noise level (95%) evaluated using statistical noise parameters such as PSNR, SNR, SSI and MSE.

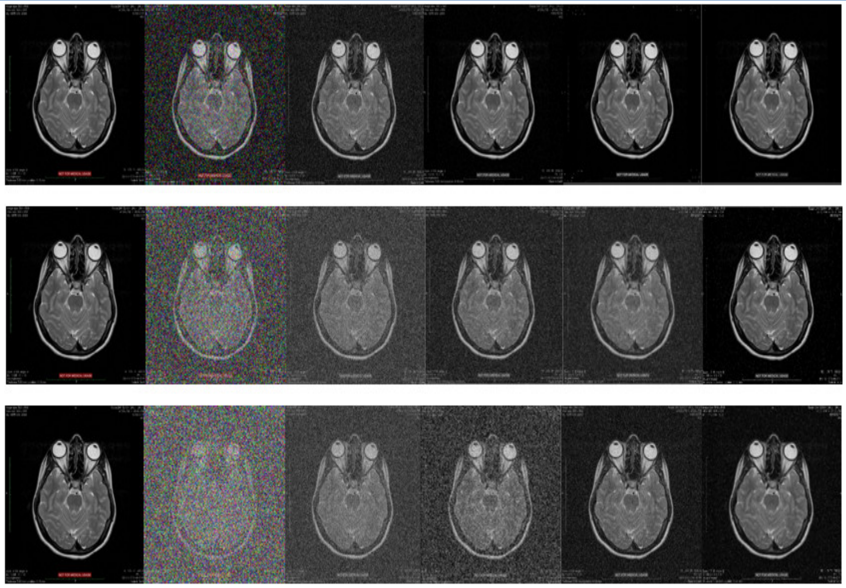

(a) (b) (c) (d) (e) (f)

Figure 5 Simulation results of different filters on brain MRI gray-scale images. Columns represents (a) Original Image, (b) Image subjected to Impulse (salt and pepper) Noise, (c) Standard Median Filter output, (d) Adaptive Median Filter output, (e) Center Weighted Median Filter output, and column (f) represents the output of Selective Weighted Median Filter (proposed filter) output. Rows represents brain MRI image corrupted with 30%, 60%, and 95% noise levels respectively. A comparison of images in column (b) with those in column (f) exhibits the enhanced pictorial quality of the corrupted images.

In this work, based on performance of image quality metrics the several noise removal algorithms have been tested. From Table I, II and III it is strong that proposed Selective Weighted Median filtering approach eliminates the noise to the maximum extent since it provides the lowest Mean Square Error (MSE) and very extraordinary Peak Signal to Noise Ratio (PSNR) values for noise level ranging between 90% to 95%. Thus the proposed approach emerge as a best and promising noise removal technique which outperforms the conventional steps for removal of substantial amount of noise present in brain MRI images and helping in preserving the edges and finest details.

Table 1: Comparative analysis of different noise removal algorithms at low noise level of 30%

Filtering Methods	Image Statistical Criterions at low Noise Level = 30%				
	PSNR	SNR	SSI	MSE	Time
Selective Weighted Median Filter	32.1812	17.2205	0.9808	3.0708	1.21
Center Weighted Median Filter	27.1089	14.1385	0.9761	9.4437	2.16
Adaptive Median Filter	26.3591	12.3910	0.8990	13.8981	1.15
Standard Median Filter	21.2810	10.3083	0.8762	15.2896	1.13

Table 2: Comparative analysis of different noise removal algorithms at low noise level of 60%

Filtering Methods	Image Statistical Criterions at Medium Noise Level = 60%				
	PSNR	SNR	SSI	MSE	Time
Selective Weighted Median Filter	24.3603	8.8675	0.5015	19.6176	1.20
Center Weighted Median Filter	22.8054	7.6578	0.3901	28.5657	2.16
Adaptive Median Filter	20.1378	5.0704	0.5127	41.6680	1.15
Standard Median Filter	18.7430	4.3803	0.2007	47.2475	1.12

Table 3: Comparative analysis of different noise removal algorithms at low noise level of 95%

Filtering Methods	Image Statistical Criterions at High Noise Level = 95%				
	PSNR	SNR	SSI	MSE	Time
Selective Weighted Median Filter	19.5222	5.7716	0.3561	27.2482	1.21
Center Weighted Median Filter	17.2665	4.2278	0.2703	37.5925	2.21
Adaptive Median Filter	16.7041	3.5551	0.1299	66.4134	1.18
Standard Median Filter	15.9743	3.1164	0.0925	74.2245	1.07

The Figures 6 – 9 demonstrates the contrast of different filters (SWMF, CWMF, AMF and SMF) performed on brain MRI image at various noise densities, in terms of PSNR, SNR, SSIM, and MSE.

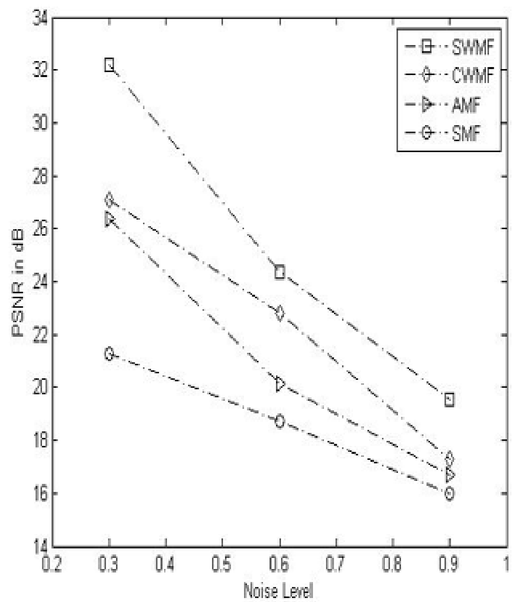

Figure 6 PSNR in dB v/s Noise Level

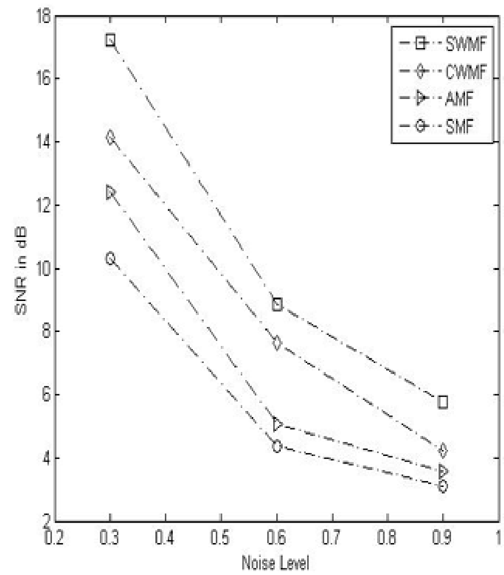

Figure 7 SNR in dB v/s Noise Level

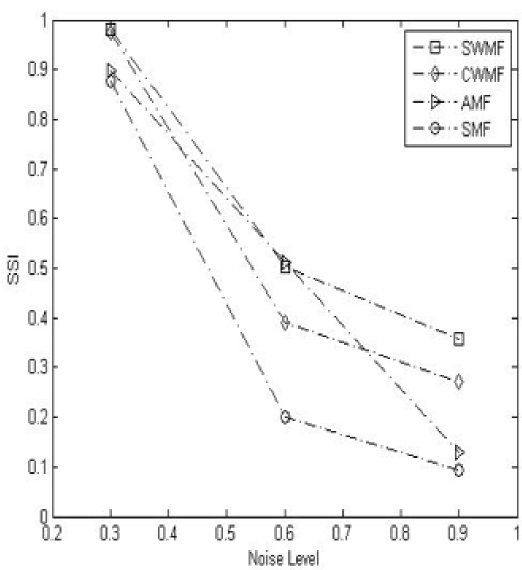

Figure 8. PSNR in dB v/s Noise Level

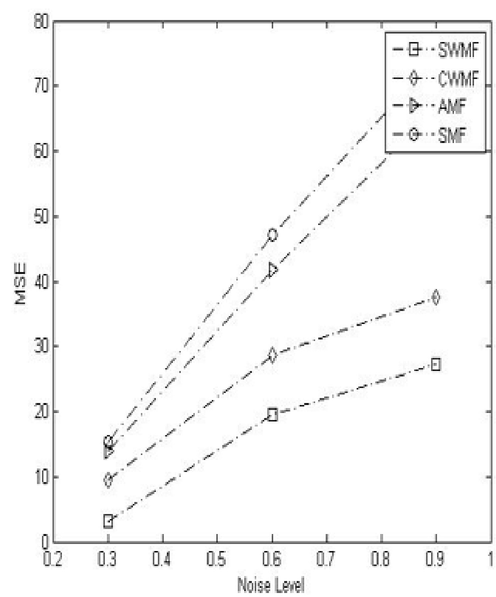

Figure 9. SNR in dB v/s Noise Level

5 Conclusion

The objective of the work is accomplished by designing and implementing the current techniques for deduction of impulse (salt and pepper) noises present in brain MRI images by providing simple and best noise filtering algorithm. In this paper we have subjected the T2 weighted real time MRI images of brain for estimating and suppressing the impulse noise using a proposed novel approach of filtering called as Selective Weighted Median filter. This work includes subsequent preprocessing steps of noise detection, grayscale conversion, and noise removal in brain MRI images. The comparative analysis of various noise removal algorithms shows that proposed algorithm provides a good results with high PSNR, SNR and low MSE values for the noise level nearly up to 95%. The results are obtained based on image evaluation criteria which is evaluated using noise statistical parameters such as PSNR, SNR, SSI and MSE. The proposed work has achieved remarkable results which helps in choosing the accurate filtering technique. And the effort can be further studied to enhance the results even when noise level increases beyond 95% by preserving the finest details very well.

REFERENCES

[1] M. a. Yousuf and M. N. Nobi, “A New Method to Remove Noise in Magnetic Resonance and Ultrasound Images,” J. Sci. Res., vol. 3, no. 1, 2011.

[2] Chan, R.H., Ho, C.W., and Nikolova, M, “Salt-and-pepper noise removal by median-type noise detectors and detail-preserving regularization,” IEEE Trans. Image process, pp. 1479-1485, 2005.

[3] Madhu S. Nair, K. Revathy, and Rao Tatavarti, “Removal of Salt-and Pepper Noise in Images: A New Decision-Based Algorithm”, Proceedings of the International Multi Conference of Engineers and Computer Scientists 2008 Vol I IMECS 2008, 19-21 March, 2008, Hong Kong.

[4] Sajjad Mohsin, Sadaf Sajjad, Zeeshan Malik, and Abdul Hanan Abdullah, “Efficient Way of Skull Stripping in MRI to Detect Brain Tumor by Applying Morphological Operations, after Detection of False Background”, International Journal of Information and Education Technology, Vol. 2, No. 4, August 2012.

[5] K. S. Srinivasan, D. Ebenezer, “A New Fast and Efficient Decision- Based Algorithm for Removal of High-Density Impulse Noises,” IEEE Signal Processing Papers, Vol. 14, No. 3, pp. 189-192, March 2007.

[6] H. Hwang and R. A. Haddad, “Adaptive median filters: New algorithms and results,” IEEE Trans. Image Process., Vol. 4, No. 4, pp. 499–502, Apr. 1995.

[7] Geoffrine Judith.M.C, and N.Kumarasabapathy. “Study and analysis of impulse noise reduction filters”, Signal & Image Processing: An International Journal (SIPIJ), Vol.2 (1), pp.82-92, 2011.

[8] Anjanappa C and Sheshadri H.S., “Comparative Analysis of Efficient Impulse Noise Removal Techniques applied to Medical Images based on Mathematical Morphology”, International Research Journal of Medical Sciences ISSN 2320 –7353 Vol. 3(9), 1-12, September (2015).

[9] B. Kwan and H. Kwan, "Impulse noise reduction in brain magnetic resonance imaging using fuzzy filters," World Academy of Science, Engineering Technology, vol. 60, pp. 1194–1197, 2011.

[10] E. George and M. Karnan, "MRI Brain Image Enhancement Using Filtering Techniques", International Journal of Computer Science & Engineering Technology (IJCSET), ISSN: 2229-3345 Vol. 3 No. 9 Sep 2012.

[11] K. Somasundaram, T.Kalaiselvi, "Automatic brain extraction methods for T1 magnetic resonance images using region labeling and morphological operations", Computers in Biology and Medicine 41 (2011) Elsevier Ltd, pp. 716–725

[12] Chih-Yuan Lien, Chien-Chuan Huang, Pei-Yin Chen, Yi-Fan Lin, "An Efficient Denoising Architecture for Removal of Impulse Noise in Images", IEEE Transactions on Computers, vol.62, no. 4, pp. 631-643, April 2013, doi:10.1109/TC.2011.256

[13] I. Shanthi, Dr. M.L. Valarmathi, "Speckle Noise Suppression of SAR Color Image using Hybrid Mean Median Filter", International Journal of Computer Applications (0975 – 8887) Volume 31– No.9, October 2011

[14] Anisha K K and Dr.M.Wilscy, "Impulse Noise Removal from Medical Images Using Fuzzy Genetic Algorithm", The International Journal of Multimedia & Its Applications (IJMA) Vol.3, No.4, November 2011.

[15] Jin Hyuk Hong, Sung Bae Cho and Ung Keun Cho (2009) "A Novel Evolutionary Method to Image Enhancement Filter Design: Method and Applications", IEEE Transactions on Systems, Man and Cybernetics – Part B, Cybernetics, Vol. 39, No. 6, pp. 1446—1457.

[16] Sung JeaKo and Yong Hoon Lee (1991) "Center Weighted Median Filters and their application to Image Enhancement", IEEE Transactions on Circuits and Systems, Vol 38, No 9.

[17] Chen C., Wng J., Quin W. and Dong X., "A new adaptive weight algorithm for Salt and Pepper noise removal", Consumer Electronics, Communication and Networks, pp.26-29, 2011.

[18] Kenny K.V. Toh and Nor A.M. Isa., "Noise adaptive fuzzy switching median filter for Salt-and- Pepper noise reduction", IEEE signal processing letters, Vol.17 (3), pp.281-284, 2010

[19] M.Ramesh, P.Priya, Punal.M.Arabi, "A Novel Approach for Efficient Skull Stripping Using Morphological Reconstruction and Thresholding Techniques", International Journal of Research in Engineering and Technology eISSN: 2319-1163 | pISSN: 2321-7308, Volume: 03 Issue: 01 Jan-2014

[20] K.Somasundaram, and R.Siva Shankar, "Skull stripping based on clustering and curve fitting with quadratic equations", ICMMSC, CCIS 283, PP 439-444. Springer – Verlag Berling Heidelberg 2012.

[21] R.C.Gonzales amd R.E.Woods, Digital image processing, Second edition, Prentice Hall, 2002.

[22] Rosniza Roslan, Nursuriati Jamil and Rozi Mahmud, "Skull Stripping Magnetic Resonance Images Brain Images: Region growing versus Mathematical Morphology", International Journal of Computer Information Systems and Industrial Management Applications, Vol 3, pp 150-158, 2011.

Society for Science and Education United Kingdom

JBEMi JOURNAL OF BIOMEDICAL ENGINEERING AND MEDICAL IMAGING

ISSN: 2055-1266
Volume 4 Issue 5

Surface Vs Volume Based Reconstruction of Bone Tissue Using CAS_Annotate and CAS_Navigate

[1,2]João Fradinho Oliveira
[1]C3i/Instituto Politécnico de Portalegre, Portalegre, Portugal;
[2]CIAUD/Faculdade de Arquitectura, Universidade de Lisboa, Lisboa, Portugal;
jfoliveira@estgp.pt

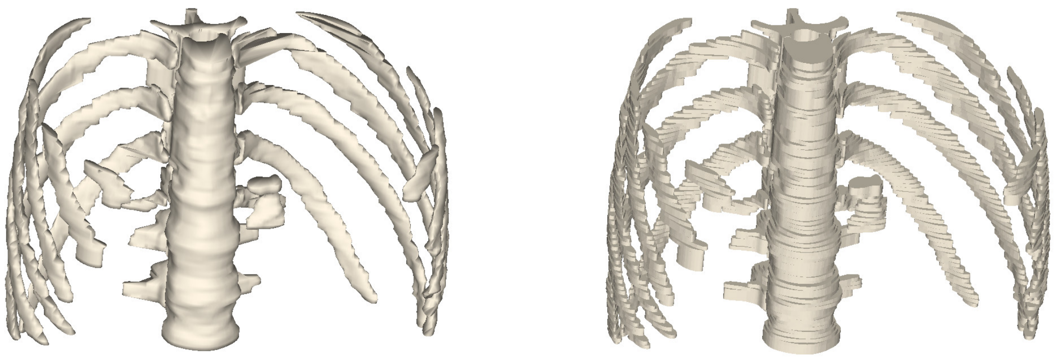

Figure 1–Reconstruction of a pig rib cage left) surface 250412 triangles; right) volume-based 498116 triangles

ABSTRACT

Intra-operative systems that provide 3D spatial reasoning support, require 3D models whose geometric accuracy enables the surgeon to make relative positioning and orientation decisions of anatomical structures during navigation. This paper compares the advantages and disadvantages of two popular types of 3D reconstruction from CT polygons, surface based and volume based respectively (Figure 1). Both are implemented in the CAS_Annotate tool, and were used for the purpose of assessing bone tissue modeling strategies for navigation. Their impact in rendering performance is assessed in CAS_Navigate which draws on IGSTK's intra-operative visualization capabilities.

Keywords: Bone tissue modeling; Image guided surgery; 3D reconstruction; VTK; IGSTK.

1 Introduction

Reconstruction of anatomical structures from planar contours presents some interesting modeling questions such as the contour correspondence and branching problem between polygons on adjacent CT slices [1], in other words, determining when an object starts, ends, joins or splits. The choice of the level of detail modeling which is adequate for a given application is also important to address. Can an object such as a vascular network be represented as a composition of several individual volume blocks?

DOI: 10.14738/jbemi.45.3771
Publication Date: 29th October, 2017
URL: http://dx.doi.org/10.14738/jbemi. 45.3771

Or does one need an object to be represented as a whole entity, for example to simulate the removal of an entire individual vertebra?. For many applications using vascular structure models such as resection mapping or approximate blood volume calculations, a volume-block reconstruction [2, 3] has eliminated all together the task of inferring or correcting connections. Similarly, organs can be a composition of surfaces, together volume-blocks (vascular networks) and composite surfaces (organs) [3] can greatly simplify the modeling task. The question this work addresses, is which of the two reconstruction approaches is preferable for basic bone visualization in an image guided surgery application?.

Before analyzing both approaches, two important factors which are intrinsic to CT and affect both are highlighted. Figure 2, shows the result of manual segmentation of the rib bone structure of a pig, using two different intensity/contrast thresholds. Often a radiologist needs to resort to two settings to infer and delimit a faint contour, making this process time-consuming. Automatic segmentation of anatomical structures in general is a very active area of research, where the comparison of algorithm results on public data sets [4] is essential to further improve and disseminate results.

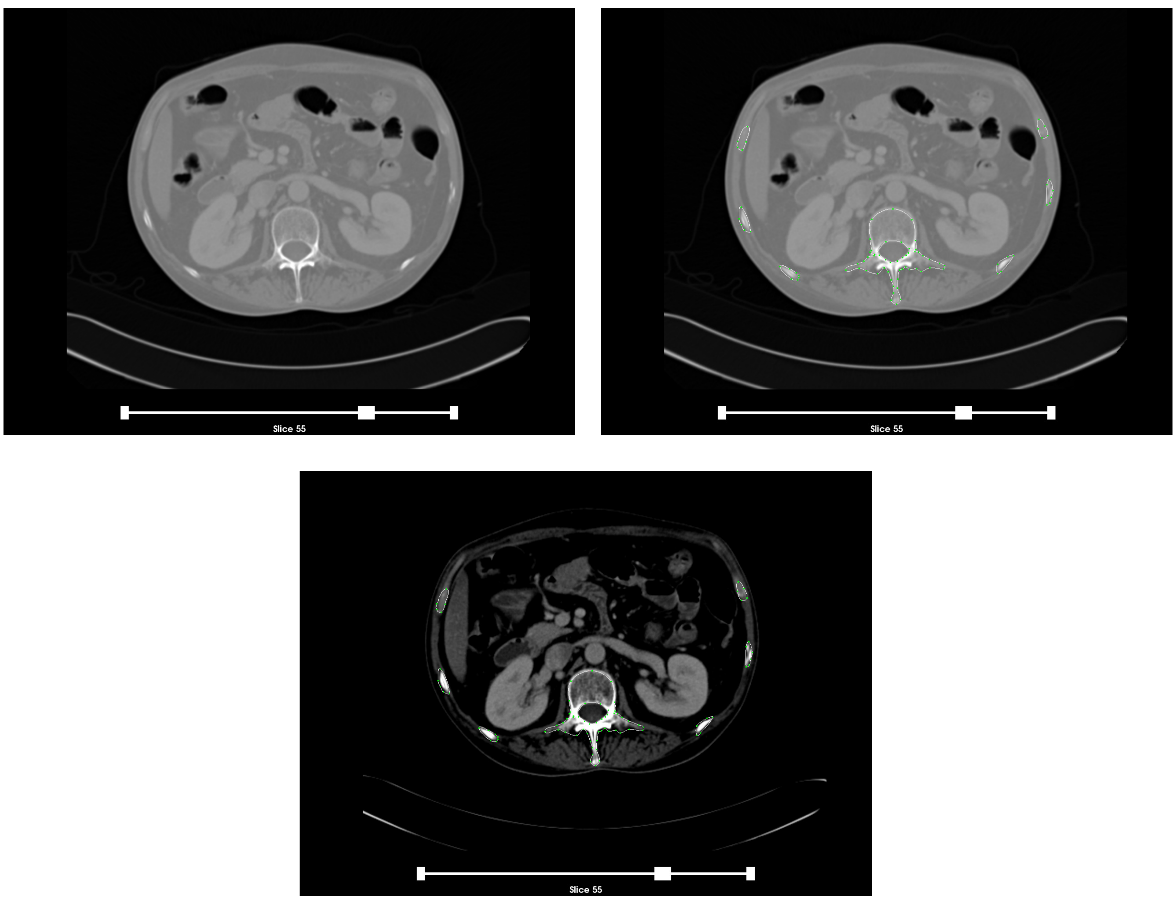

Figure 2 – Segmentation of bone tissue polygon contours with CAS_Annotate. Top left: original slice; Top right: image threshold T1; Bottom right: image threshold T2

The second factor, is the problem of limited resolution between CT slices. The drastic shape difference between adjacent contours (Figure 3) may or may not indicate a new object.

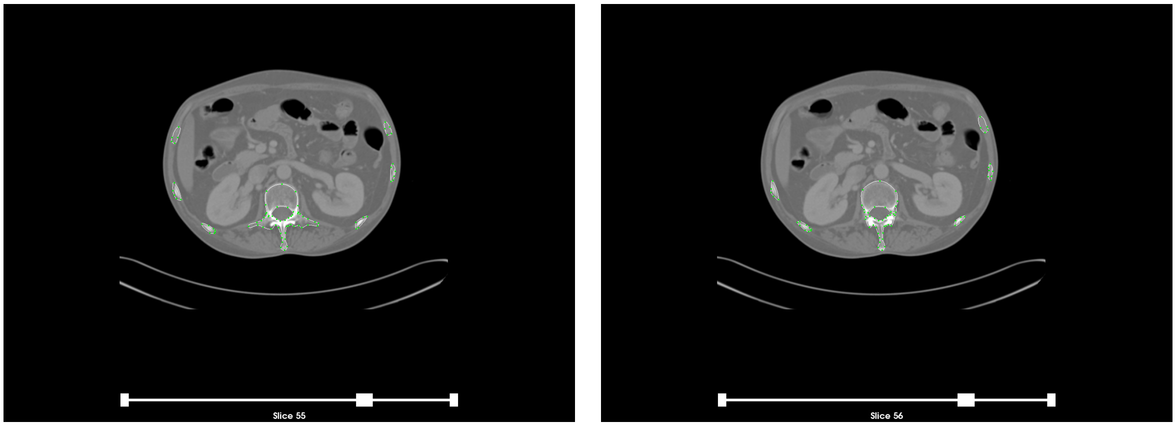

Figure 3 – Drastic shape variation between adjacent slices.

2 Materials and Methods

The following diagram (Figure 4) illustrates the main components of the CAS_Annotate and CAS_Navigate tool.

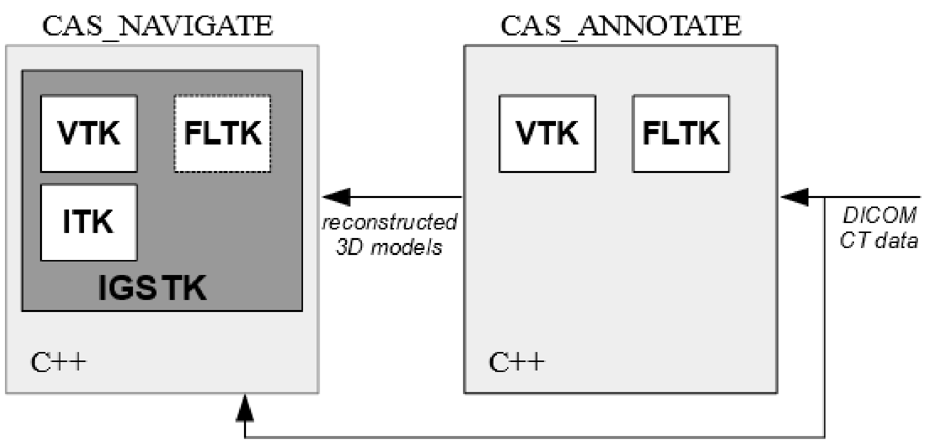

Figure 4 – CAS_Annotate and CAS_Navigate system components

CAS_Annotate uses VTK [5] functionality to: read and display DICOM [6] images (vtkImageViewer2), manually create and edit a polygon contour (vtkContourWidgets). The system uses FLTK [7] to create a user interface that among other functionality allows to select a DICOM image dataset from disk, write and read polygon contours and their correspondences following the file format detailed in [3]. Volume-based reconstruction does not require any polygon correspondences, but surface reconstruction does. Creating a correspondence between two polygons can be done simply by right clicking near a polygon, pressing ´c´, change the slice being viewed, right clicking near the corresponding polygon and pressing 'v'. Once all contours have been created and relevant links established one can choose to create a volume-based reconstruction or a surface reconstruction. With a volume-based reconstruction, every polygon is copied onto the next adjacent slice, with this 1-1 correspondence, vertices from both polygons are simply triangulated and the top and bottom side of the volume block are closed using Eberly's triangulation by ear-clipping algorithm [8]. For the surface reconstruction, the system uses Eberly's triangulation when a polygon contour has no polygon correspondence links either above or below. Corresponding polygons in adjacent slices are tilled together using Christiansen and Sederberg algorithm [9] which allows for a different number of vertices to exist in each polygon and also supports an elegant bifurcation solution. Finally, it is also possible to create either a high or low resolution version of a reconstruction, the later extracts only the control points of the spline vtkContourWidgets. For more details please refer to [10]. Once the models have been created, they can be saved in either the PLY format [11] or IGSTK's [12] 3D .Msh object file format.

CAS_Navigate uses IGSTK to read and render efficiently the created 3D models over the DICOM images [13] and to connect surgical trackers.

3 Results and Discussion

A Sony Vaio laptop computer with an Intel i7 2.80Ghz processor, 6 GB RAM, and an AMD Radeon 6630M graphics acceleration card was used for the reconstruction and visualization. Whilst the reconstruction of automatically or previously segmented polygons is possible with CAS_Annotate (provided that the polygon vertices follow the contour file layout detailed in [3]), manual segmentation was performed for the polygons in this study. Specifically a 74 slice CT dataset of the rib cage and spine of a pig was chosen, and 715 contour polygons were segmented with a total of 7105 control vertices (some contour polygons are visible in Figure 2 and 3).

Low and high resolution models were created for both the surface based reconstruction and the volume based reconstruction. The surface reconstruction, created 19 separate objects using one contour-link file. Incomplete contours, with less than 3 vertices were ignored. Every reconstructed models was created in less than one second. It took approximately 50 minutes to manually establish the contour links, and just under 5 hours to annotate the 715 polygons. Table 1 outlines the model complexity of the four created datasets, the models are shown in Figure 5 with flat rendering on the left column, and wireframe with flat rendering on the right column.

Table 1 – Model complexity

Model	#Triangles	#Vertices
low_res_block_model	25472	14166
low_res_surface_model	14090	7083
high_res_block_model	498116	250488
high_res_surface_model	250412	125244

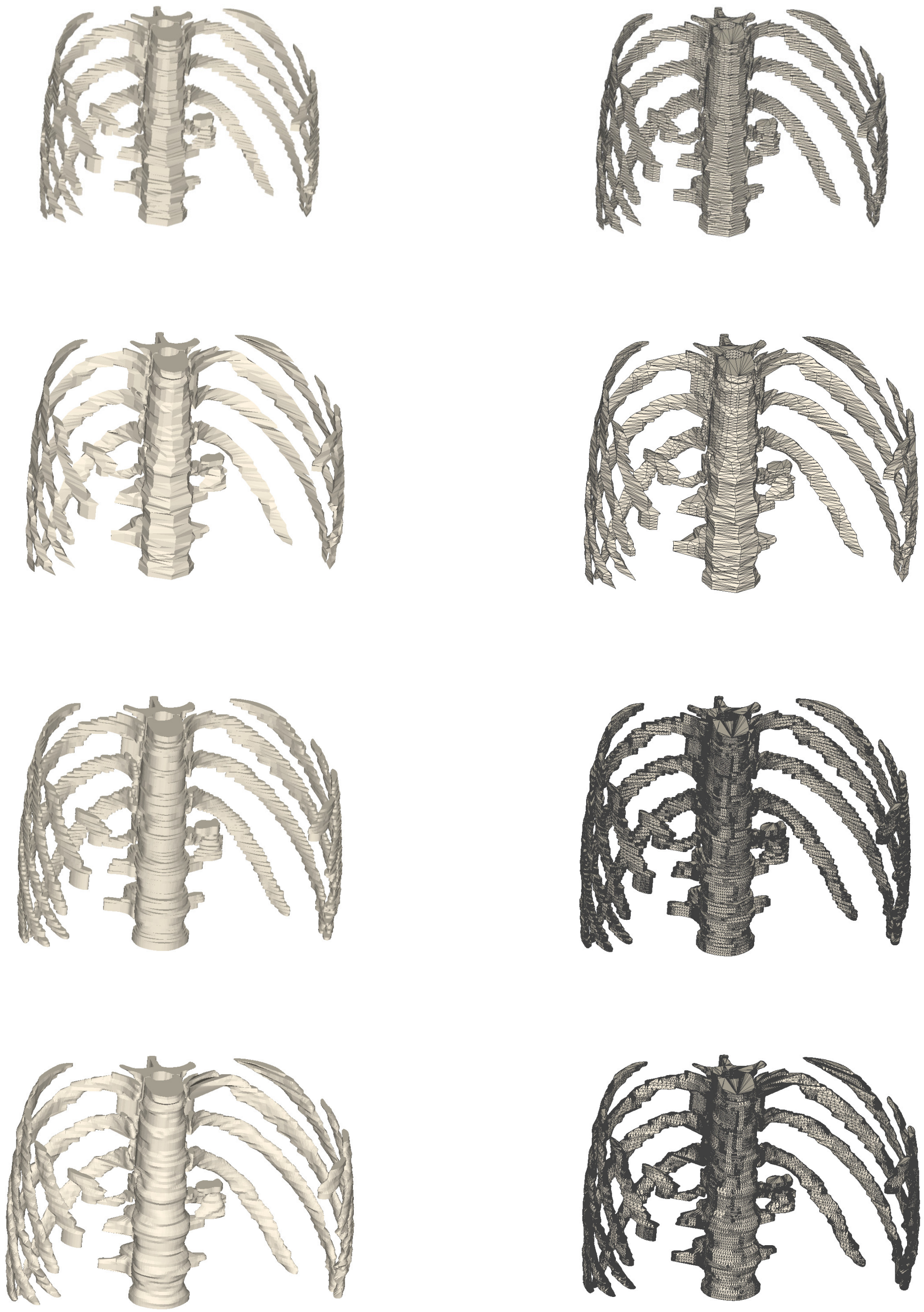

Figure 5 – Model results (left: flat shading, right: flat shading and wireframe rendering) – from top to bottom: low_res_block_model, low_res_surface_model, high_res_block_model, high_res_surface_model.

The first observation of the results, is that the surface based reconstruction generates off-axis geometry which make the created models visually "smooth" in all view angles, whereas the volume-based reconstruction has some view angles where the regular axis aligned structure is more apparent (top row, and third row from top). Another observation is that the higher resolution versions "inflate" the models in some areas, more noticeably on the top edge region of the ribs, this occurs as a result of more vertices becoming available to represent the curve. Figure 6, shows rendering artifacts in the lower left area of the spine on both the low and high resolution surface reconstruction, whilst the volume-based approach on the top right corner has no such artifact. With closer inspection, the artifact results from the surface reconstruction creating long triangles in an effort to stitch two very different polygon contours (as illustrated in Figure 3). One way to alleviate this problem would be to detect during the reconstruction slices that generate long triangles, and generate intermediate intra-slice interpolated contours. It should also be pointed out that the individual vertebra were not modeled as separate objects, rather the spine was created as two continuous structures. Modeling each vertebra individually is a simple matter of not creating links between links before and after the corresponding polygons. However, vertebra do not align with the slices, and it becomes difficult to define when does one begin, and another end.

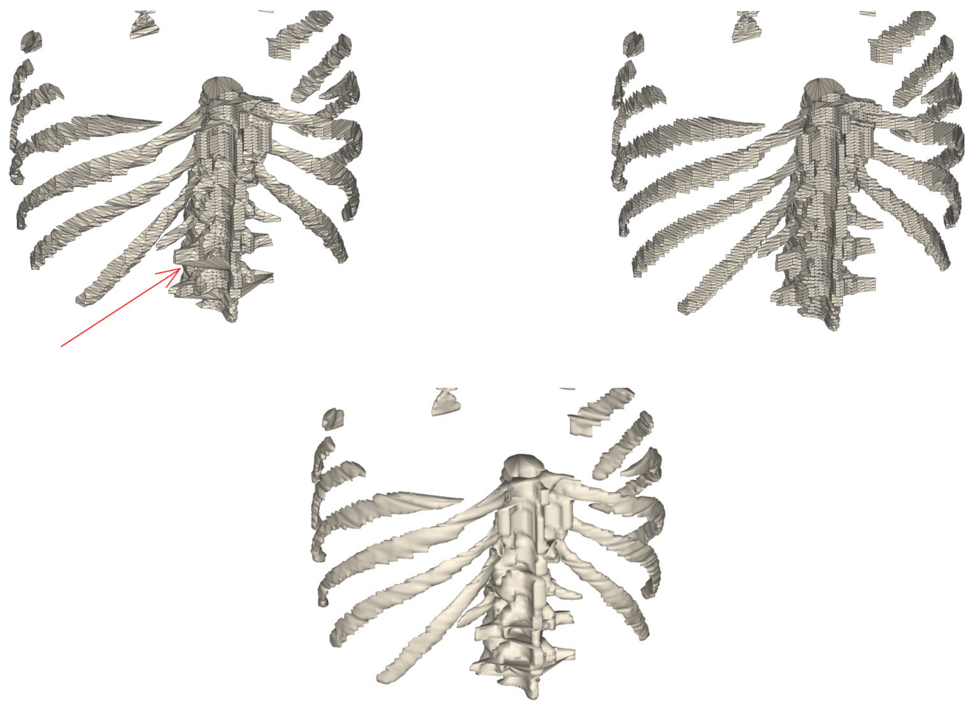

Figure 6 – Drastic shape variation between slices - Surface based reconstruction (left column) Vs Volume based reconstruction (right) – topleft: low_res_surface_model; topright: low_res_block_model; bottom left: high_res_surface_model.

The generated models were loaded in CAS_Navigate, along with models of the liver and vascular structures (Figure 7), and all resolutions (Table 2) rendered at smooth interactive rates. The vascular structures (volume-based reconstruction) and bone models (surface based reconstruction) were set to completely opaque, whilst the organs (surface based reconstruction) had opacity/alpha blending set to 0.4.

.

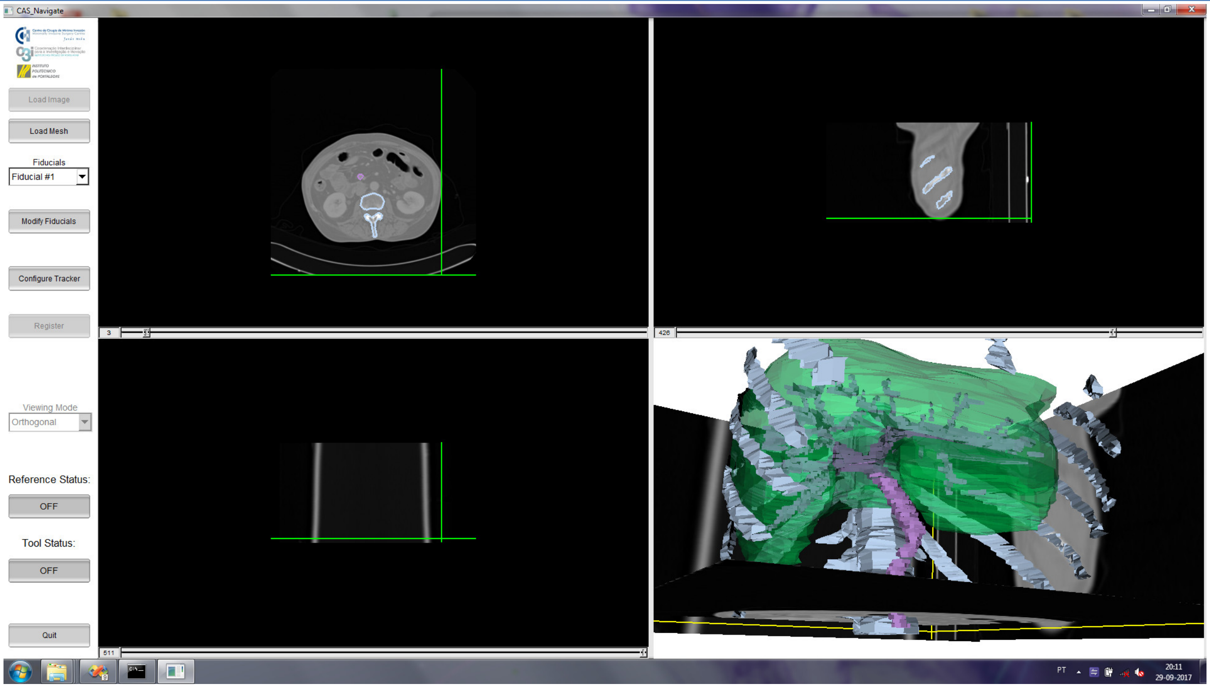

Figure 7 – Volume-based reconstructed model (veins) and surface based reconstructed models (liver+bones) visualization in CAS_Navigate

Table 2 – Model complexity

#	Model	Type of Reconstruction	Resolution	#Triangles	#Vertices
1	Liver2 (composite surface)	surface	low	3248	1626
2	Liver2b (composite surface)	surface	low	550	277
3	Vascular network	volume	low	7572	4388
4	Rib cage (low_res_surface_model)	surface	low	14090	7083
5	Rib cage (high_res_block_model)	volume	high	498116	250488
	Total A (1+2+3+4)	-	-	25460	13374
	Total B (1+2+3+5)	-	-	509486	256779

4 Conclusions

The volume-based reconstruction by definition limits the maximum horizontal and vertical geometric error of the model to be the space between slices. This is particularly useful, as drastic polygon shape changes in adjacent slices might generate some rendering artifacts in a surface-based reconstruction. The surface reconstruction required 50 more minutes than the volume-based reconstruction for the user to manually define where the 19 objects started and ended. Further defining where each vertebra starts and ends could potentially solve the rendering artifacts in the surface approach, but requires more user time, and it could be potentially difficult to establish as vertebrae are not scan aligned.

Finally, for the purposes of navigation, inspection of vascular structures of a liver, the artifacts did not pose a problem as they are small and localized. Either volume-based or surface-based reconstruction gave the geometric spatial context desired to inspect the liver and vascular networks.

ACKNOWLEDGMENTS

This work was partially funded by Programa de Cooperación Transfronteriza España-Portugal (POCTEP), Fondo Europeo de Desarrollo Regional (FEDER) 0401_RITECA_II_4_E.

REFERENCES

[1] Meyers D, *Reconstruction of Surfaces from Planar Contours.* PhD Thesis. University of Washington, 1994.

[2] ITK, *ITK-Snap*, http://www.itksnap.org, 2017.

[3] Oliveira, J. F. , J. L. Moyano-Cuevas, J. Blas, H. Capote, and F. M. S. Margallo, *Preoperative and Intraoperative Spatial Reasoning Support with 3D Organ and Vascular Models: Derived from CT Data using VTK and IGSTK*, International Journal of Creative Interfaces and Computer Graphics, vol. 6(2), pp. 56–82, July-December, 2015.

[4] Sliver, http://www.sliver07.org, 2017.

[5] The Visualization Toolkit, http://www.vtk.org, 2017.

[6] Pianykh, O. S., *Digital Imaging and Communications in Medicine (DICOM) A Practical Introduction and Survival Guide*, 2nd Edition, Springer, ISBN 978-3-642-10849-5, 2012.

[7] The Fast Light Toolkit (FLTK), www.fltk.org, 2017.

[8] Eberly D, *Triangulation by Ear Clipping, http://www.geometrictools.com,* 2008.

[9] Christiansen HN, Sederberg TW, *Conversion of complex contour line definitions into polygonal element mosaics*. Computer Graphics XIII. 2(August, 1978):187-192, 1978.

[10] Oliveira, J. F., *Advantages and Disadvantages of using Third-party software in the development of the CAS_Annotate and CAS_Navigate Medical Applications*, Journal of Biomedical Engineering and Medical Imaging, 3(6), ISSN: 2055-1266, 2016.

[11] The Stanford 3D Scanning Repository, Stanford University, http://graphics.stanford.edu/data/3Dscanrep/, 2017.

[12] The Image-Guided Surgery Toolkit, http://www.igstk.org, 2017.

[13] Insight Segmentation and Registration Toolkit (ITK), https://itk.org, 2017.

SOCIETY FOR SCIENCE AND EDUCATION
UNITED KINGDOM

JBEMi JOURNAL OF BIOMEDICAL ENGINEERING AND MEDICAL IMAGING

ISSN: 2055-1266
VOLUME 4 ISSUE 5

Approach to Detecting Forest Fire by Image Processing Captured from IP Cameras

[1]Tran Quang Bao, [2]Nguyen Thi Hoa

[1] *Department of Environment Management, Vietnam National University of Forestry, Vietnam*

[2] *Department of Resources and Environment, Vietnam National University of Forestry at Dong Nai.*

baofuv@vfu.edu.vn; hoanguyen.nrm@gmail.com

ABSTRACT

In this paper, the results show an algorithm to detect the presence of smoke and flame using image sequences captured by Internet Protocol (IP) cameras is represented. The important characteristics of smoke such as color, motion and growth properties are employed to detect fire. For the efficient smoke and fire detection in the captured images by the IP camera, a detection algorithm must operate directly in the Discrete Cosine Transform (DCT) domain to reduce computational weigh, avoiding a complete decoding process required for algorithms that operate in spatial domain. In order to assess the possibility and the accuracy of proposed algorithm, the author used the video sequences which are captured by IP camera from control forest fire at different spatial location and levels of fire intensity. Evaluation results illustrated the efficiency of the proposed algorithm in effectively detecting forest fires with accuracy at 97%.

Keywords: Forest fire; Smoke and Fire Detection; DCT; IP Camera; Images Processing

1 Introduction

Forest fire is a complex physiological process which includes numerous direct and indirect impacts on the atmosphere, biosphere and hydrosphere. That is one of the key drivers of major changes in term of air pollution in many parts of the world. Forest fires often occur on a large scale especially in complex mountainous terrain, intricate to access. Therefore, forest fire detection by traditional approaches is inappropriate.

In recently years, Vietnam annually has 650 forest fires which are damaged average 4.340 ha of forest. In which, it has about 3.200 ha plantation forest and approximately 1.140 ha of natural forest. In 2002, forest fires in U Minh Thuong and U Minh Ha destroyed 5.500 ha of Melaleuca forest, including 60% of primary forest. In early 2010, forest fires in Hoang Lien - Lao Cai National Park destroyed more than 700 ha of forest. The deprivations caused by forest fires in term of economic, social and environmental are quite enormous and difficult to calculate.

Early detection of forest fires can help to alarm and prevent disasters, resulting in major human and property damage. The combustion of objects usually begins with the emission of smoke, even before igniting. Therefore, smoke is an essential element for early fires detection. The smoke characteristics depend on the chemical properties, temperature, oxygen content, etc. The color of the smoke ranges

DOI: 10.14738/jbemi.45.3856
Publication Date: 29th October, 2017
URL: http://dx.doi.org/10.14738/jbemi. 45.3856

from white to white-blue when fired at low temperatures and from gray to black when the temperature rises to ignition. The most general smoke detectors are based on infrared or ultraviolet cameras. In addition, other detection techniques are based on particle analysis, temperature, relative humidity, and air transpiration. These systems will operate when smoke or fire particles are close to fire detection devices and unable to provide information regarding the exact location, intensity, spread, etc. [1] To provide more accurate and reliable smoke detection, some video-based detection systems have been proposed. The algorithm for detecting fire through video is based on two main characteristics of fire: flame and smoke. Most fire detection algorithms in the theory use some of the characteristics of fire and smoke, such as fire / smoke color, flaking, changing of fire area boundary.

Recently, the use of IP cameras with video surveillance has grown significantly, due to the simple IP-based monitoring system at low cost. Therefore, the use of cable systems and wireless Internet infrastructure has been widely applied [3]. Furthermore, an IP camera not only captures sequences of images but also has its own processor, memory and operating system, allowing programs to process information obtained without additional computer equipment. IP cameras can be connected to form networks that make a video surveillance system more reliable. Data is the information provided by encrypted IP cameras in many format: Motion-JPEG (MJPEG), H.264, or so on… [3].

This paper focuses on image processing techniques based on the use of smoke detection algorithms from IP camera. Proposed algorithms operate directly in the DCT domain and can be implemented on IP camera surveillance systems. This algorithm has used a number of smoke features including color, motion and spread characteristics that extracted directly from the DCT coefficient during decoding.

2 Materials and Methodology

2.1 Forest fire detection algorithm for IP camera

2.1.1 IP camera – image receiver

The use of IP technology for forest fire detection give a countless advantage, for example IP-camera networks can detect fire origin magnitude and propagation in more accurate manner compared with a single video surveillance system. However, to efficiently use the IP technology for fire detection purposes, the smoke detection algorithm must perform directly in the Discrete Cosine Transform (DCT) domain, because decoding (from DCT domain to spatial domain) and possible encoding (from spatial domain to DCT domain) are considerably high time consuming processes. Moreover, almost all fire detection algorithms including those proposed in [2, 5, 6] are carried out in the spatial domain, analyzing the value of each pixel or block of pixels. Therefore, any implementation of these algorithms in IP technology requires considerably high extra processing time.

Generally, an IP camera captured sequences of images, the number of frame captured depend on each different camera, normally it can reach over 20 frames per second. In addition, has its own processor, memory and operating system, allowing loaded programs to process the captured information without the need of additional computer equipment and the information provided by IP camera is encoded data in JPEG or MJPEG format.

Additionally, the quality of images captured by IP camera is stable without disturbance by signal transmission process. For normal cameras which are set up in less interfering environment and the signal is transmitted by coaxial cable to the receiver, signal still affected by material of it's cable. Therefore, the quality of images cannot be remaining for analysis process to detect objects, particularly forest fires.

2.1.2 Image processing to detect forest fires

Normally, IP camera uses two basic protocols to access the images that captured from the sensor via internet: *http* protocol (HyperText Transfer Protocol) and *rtsp* protocol (Real Time Streaming Protocol). These protocols allow access data from IP camera in two different formats: (1) *http* protocol allows assess and download directly JPEG images; (2) *rtsp* protocol uses H.264 codec, thus the received signal need a decoder to covert it ino JPEG images. Each protocol is used depending on different IP camera. Captured images by IP camera would be sort by time and then put in image processor to detect smoke or flame or event both of these signals (see fig. i).

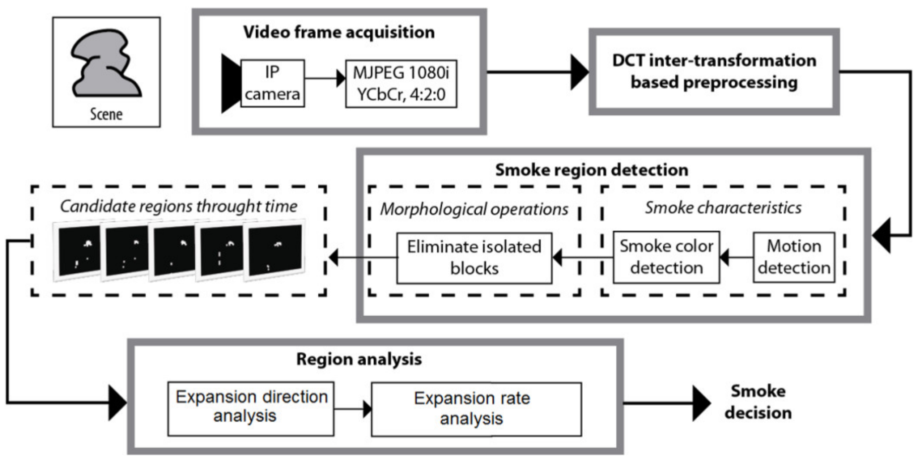

Figure 1. Block diagram of the proposed smoke detection scheme (Leonardo et al, 2012)

Captured images from IP camera usually have relatively high resolution and the minimum resolution is 1280 x 720 px. If these images are processed directly, the processes are highly time consuming operations but high accuracy. By contrast, if these images are zoom out, the processing time requires less but low accuracy. To detect forest fire, it is not requiring high speed but need high accuracy, thus the captured images will be remaining quality for processing.

In this paper, the author not establish a new algorithm for image processing, they use the combination of many algorithms that are applying in detecting forest fire in the world [2, 4]. Including:

The image that captured by camera is divided into blocks of 8 x 8 pixels of each frame. After that, the DCT inter-transformation is applied to all DCT blocks of 8 × 8 coefficients of each frame to get DCT blocks of 4 × 4 coefficients. Using the DC values of each DCT block of the 4 × 4 coefficients of several consecutive frames, motion and color properties of smoke are analyzed to get the smoke region candidates. Each DCT block can define 3 channels including Y, Cb and Cr. In which, to identify the motion of DTC blocks, the author use channel Y, and to classify the characteristics color of smoke and flame use channel Cb and Cr.

- *Motion detection*: Consider the DC coefficients of block DCT block of S_b x S_b (S_b = 8), this coefficient is the value to analyze the characteristics of motion of a block. S_b times the average value of the block in spatial domain which is given by:

$$C(0,0) = \sqrt{\frac{2}{S_b}}\alpha(0)\sum_{q=0}^{S_b-1}\left(\sqrt{\frac{2}{S_b}}\alpha(0)\sum_{q=0}^{S_b-1}B(p,q)cos\left(\frac{(2p+1)\times 0\times\pi}{2S_b}\right)\right)\cos\left(\frac{(2p+1)\times 0\times\pi}{2S_b}\right) \quad (1)$$

$$= S_b \times \left(\frac{1}{S_b^2}\sum_{q=0}^{S_b-1}\sum_{p=0}^{S_b-1}B(p,q)\right) \quad (2)$$

In which, $Y_t(x, y)$ is the DC coefficient value of a block at location (x, y) in frame *t*. Each DCT block is classified into motion or statistic block as equation below:

$$f_m\left(Y_{t-1}^{DC}(x,y), Y_t^{DC}(x,y)\right) = \begin{cases} 1\ if\ th_1 < \frac{1}{S_b}\left|Y_{t-1}^{DC}(x,y) - Y_t^{DC}(x,y)\right| < th_2 \\ otherwise \end{cases} \quad (3)$$

Considering that f_m is a binary matrix of size M × N (M is width, N is the height of captured image). And th1 and th2 are two threshold values are experimentally determined as 12 and 80 respectively which considering the general motion speed presented by smoke

-*Smoke color analysis*: color is another integral feature of smoke that have been used commonly in several smoke detection algorithms. Almost al algorithms used RGB and YcbCr (Y: Luminance; Cb: Chrominance-Blue; and Cr: Chrominance-Red) color space-based rules to determine smoke color.

+ These rules are given by equation:

$$\text{Rule 1: } R \pm \alpha = G \pm \alpha = B \pm \alpha \quad (4)$$

$$\text{Rule 2: } 80 \le (R + G + B) / 3 \le 220 \quad (5)$$

Where $15 \le \alpha \le 20$

- The pixel is considered as smoke if these adapted as follows:

$$\text{Rule 1: } (C_b - 128)^2 + (C_r - 128)^2 \le \alpha^2 \quad (6)$$

$$\text{Rule 2: } Th_3 \le Y \le Th_4 \quad (7)$$

Where C_b, C_r, Y are the DC values of two Chrominance and Luminance of (x,y) block, applying the linear transform between RGB and YCbCr, it follows that α = 10, *Th3* = 80 and *Th4* = 220. Thus, if both rules are satisfied, DCT block is considered as smoke by color property, that is $f_c = (Y, C_b, C_r) = 1$, otherwise $f_c = (Y, C_b, C_r) = 0$.

Therefore, both feature analyses are conducted, the blocks that satisfy both smoke features are considered as smoke candidate region, as follows:

$$B_t = f_m \wedge f_c \wedge f_l. \quad (8)$$

- Region analysis

After detecting smoke candidate, it necessary to eliminate some objects possess similar properties to smoke. The connection of several connection blocks is used and each candidate region is denoted by A_k, k = 1, 2, 3, … K. where *k* means the label number. Considering that smoke has a property of continuously expansion, the corresponding of two adjacent smoke regions presents an expansion overlapping. To analyze this smoke property, each region is updated using Equation:

$$A_t^k = \begin{cases} A_{t-1}^k \cup A_t^k, \text{nếu } A_{t-1}^k \cap A_t^k \neq \emptyset \\ A_t^k, otherwise \end{cases} \quad k = 1, 2, \ldots, K \tag{9}$$

In consequence, a new image includes motion region and is labeled can be considered as smoke region. On the other hand, if captured images are not satisfied with al the rules above, it is not considered a smoke region.

2.1.3 System architecture (Ground monitoring station)

An overview of the ground monitoring system is illustrated in fig. ii. The system is designed as a unified block that automatically captures images around the station.

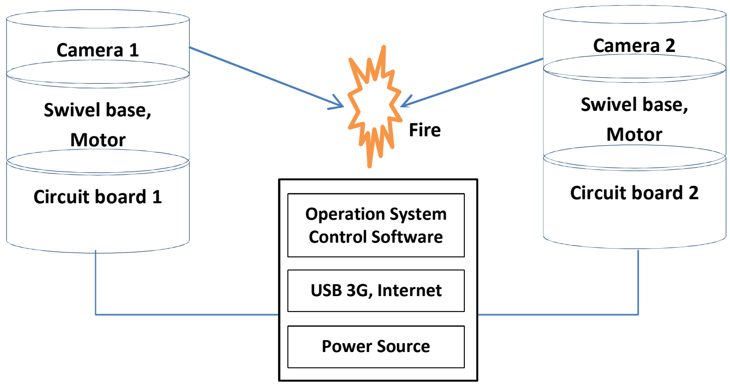

Figure 2. The block scheme of fire watch system

This system has 2 independent cameras which are rotated in a circle. All these motions are programmed to cover the area surveillance automatically by mean of repetitive sweeps. In a rotation, each camera provides 36 images evenly.

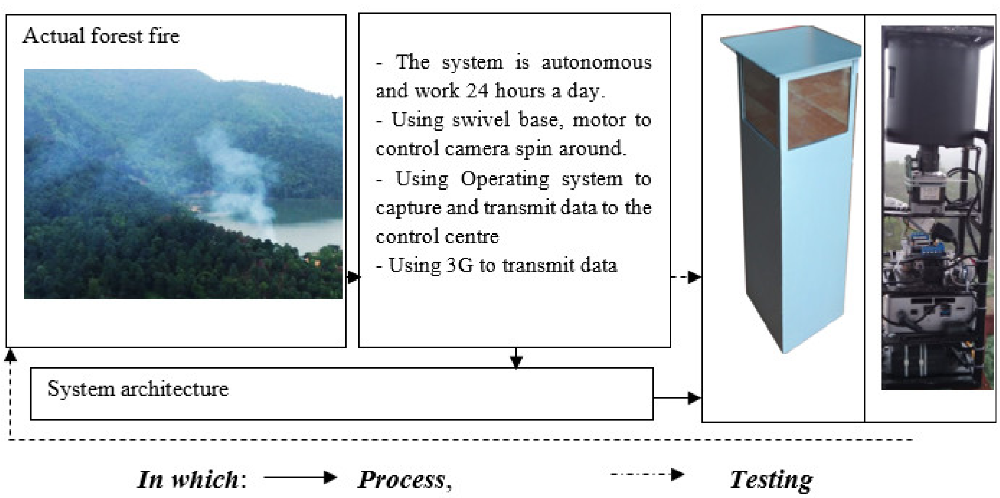

Figure 3 The diagram of the system's function

2.2 The image-based fire detection software

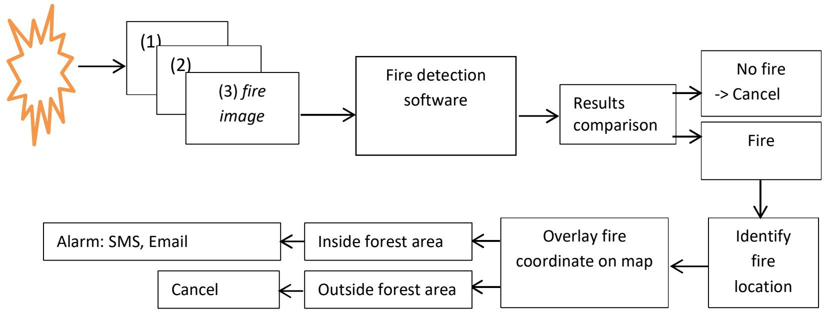

Figure 4. Block diagram of proposed fire detection software

At the same location, camera captured a number of images in different time which are processing and comparing with each other by detection algorithms to give a final result. The coordinate of fires is determined by the two integrated camera. These coordinate are overlaid with forest map, road map and hydrograph map to classify it belong to forest area or not. If the fire occurs in forest area, a fire-alarming is given immediately through email and SMS.

Combination of software and hardware in the system is illustrated in figure. 5.

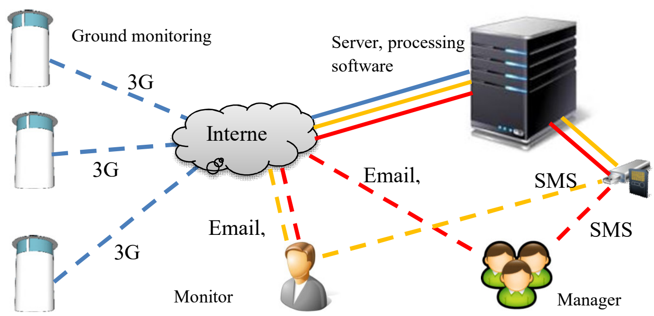

Figure 5. The forest fire detection system architecture

2.3 System operation

Each monitoring system include 01 IP camera connected to the Internet to transmit to the server by 3G signal. These data are captured images which after a predetermined period of time are retrieved automatically by software from serve for analyzing process. In the case of many stations connected to sever, this software will set up the time for assess to station in a fixed cycle that all images could be collected. There more stations connected to server the more operation in the system and the cycle is more complicated.

Each captured images will be analyzed to detect smoke and flame by some smoke or fire detecting algorithms (fig vi). When a fire is detected, system will will identify the exact it's location and give an alarm. The coordinate of a fire can be determined by coordinated of 2 monitoring stations and 2 observation angles from camera in these stations. By overlaying fire's coordinates on forest map, software will define exactly where fire occur in forest or non forest. When detected an abnormality (flame, smoke) the system will give a message to phone, email or website to warning users automatically. The manager can access and chose appropriate solutions.

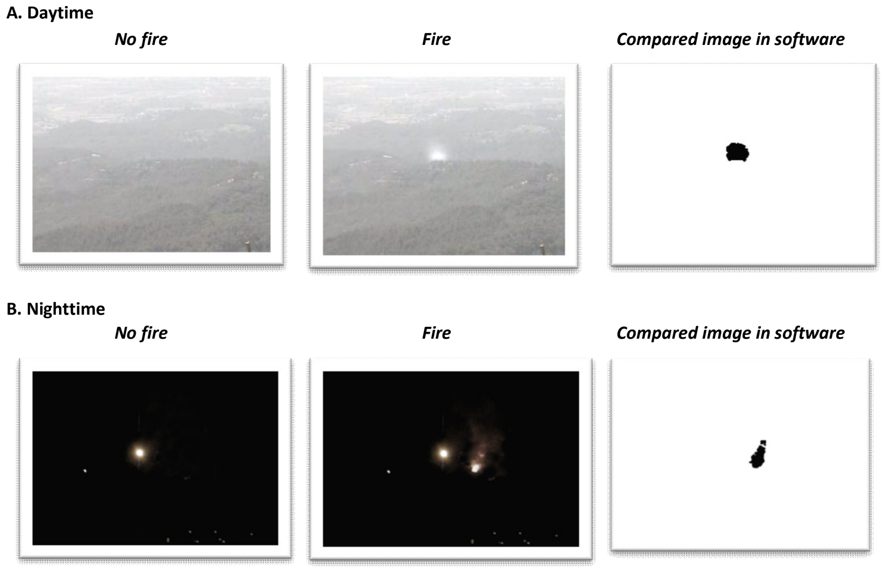

Figure 6. Captured images from camera to determined fire

Time for analyzing an image is about 0.3 second. Time for loading an image from station depends on the connection speed of 3G network. However, the image resolution is low (280 x 720 Pixel- up space of about 140 Kb), loading image is not taking too long time. Hence, a camera will load about 1440 images approximate 197 Mb in a day. These images are stored in hardware and will be delete after period of time depend on the space of hardware.

2.4 Materials

The performance of smoke, flame detection and the accuracy of proposed algorithm is evaluated by using different sample video sequences and conducted some "control burnings".

Table 1. The description some of video sequences used in evaluation of the proposed algorithm

TT	Content	Quality
1	The vertical background is crowded with vehicles, near camera has a large branch of tree that affected by strong winds.	- Video size: 320 x 240 pixel - Frame speed: 9fps - Time: 00:11:02
2	View from the hill to around in sunny condition, faint image, effected by insect, weak wind.	- Video size: 352 x 288 pixel - Frame speed: 25fps - Time: 00:04:01
3	The frame of a fire in sunny conditions, the location of fire coincides with horizon, slow fire speed, weak wind.	- Video size: 720 x 576 pixel - Frame speed: 7fps - Time: 00:02:01
4	The frame of smoke is produced by a factory in residential area which is crowded with vehicles and people, weak wind.	- Video size: 720 x 576 pixel - Frame speed: 10fps - Time: 00:01:00
5	A frame contains a "control burning" in closely distance, people walked around the fire.	- Video size: 320 x 240 pixel - Frame speed: 15fps - Time: 00:00:47
6	A frame contains a forest fire in closely distance, the image of the fire covered the frame.	- Video size: 400 x 256 pixel - Frame speed: 15fps - Time: 00:00:13

a. U Minh Thuong National Park *b. Soc Son – Ha Noi* *c. Ba Vi National Park*

Figure 7: The test image of control burning to evaluate the smoke and fire detection capabilities of proposed algorithm

3 Results and discussions

3.1 Testing proposed algorithm with video

The results of testing some video sequences indicates the performance of the proposed algorithm in detecting smoke and fire.

Table 2 The results of evaluating the accuracy of proposed algorithm in video sequences

No	Video 1		Video 2		Video		Video 4		Video 5		Video 6	
	Detected	No detected	Detected	No detected	Detected	No detected	Detected	No detected	Detected	No detected	Detected	No detected
1	532	3	180	0	49	0	24	0	130	0	154	0
2	337	6	210	1	65	1	38	0	112	0	128	0
3	465	22	191	0	51	0	39	0	168	0	153	0
4	531	7	208	1	39	1	35	1	132	0	154	0
5	531	6	177	0	35	0	32	1	149	0	130	0
6	531	7	147	0	32	1	21	0	151	0	151	0
7	401	25	206	0	21	0	21	0	162	1	154	0
8	332	36	226	1	21	0	21	0	145	0	154	0
9	216	6	238	1	23	0	23	0	122	0	154	0
10	314	8	220	0	29	0	29	1	156	1	154	0
Ave.	419	12.6	200.3	0.2	36.5	0.82	28.3	1.06	142.7	0.2	148.6	0

Table 2 shows that there is only video 01 have got a false alarm (3%), and the number of video remaining perform the rate of detecting that approach to 100 % in term of accuracy. There are some reasons that affect on false alarm in video 01. Firstly, in the video many vehicles are running in the road. The second reason is near the camera has a large branch of tree that affected by winds. In contrast, the remaining video, the objects are in static state and clearly background. This indicates that apply proposed algorithm in detecting smoke and fire is effectiveness.

3.2 Testing proposed algorithm with reality fire

The yield of proposed algorithm is calculated based on "control burning" in some areas. Fig 07 and 08 show the video sequences in evaluate performance of detecting smoke and fire algorithm, Fig (a1, a2, a3, a4 and b1, b2, b3, b4) are the frame of fire and Fig (c1, c2, c3, c4) are images after processed.

- Smoke detection results

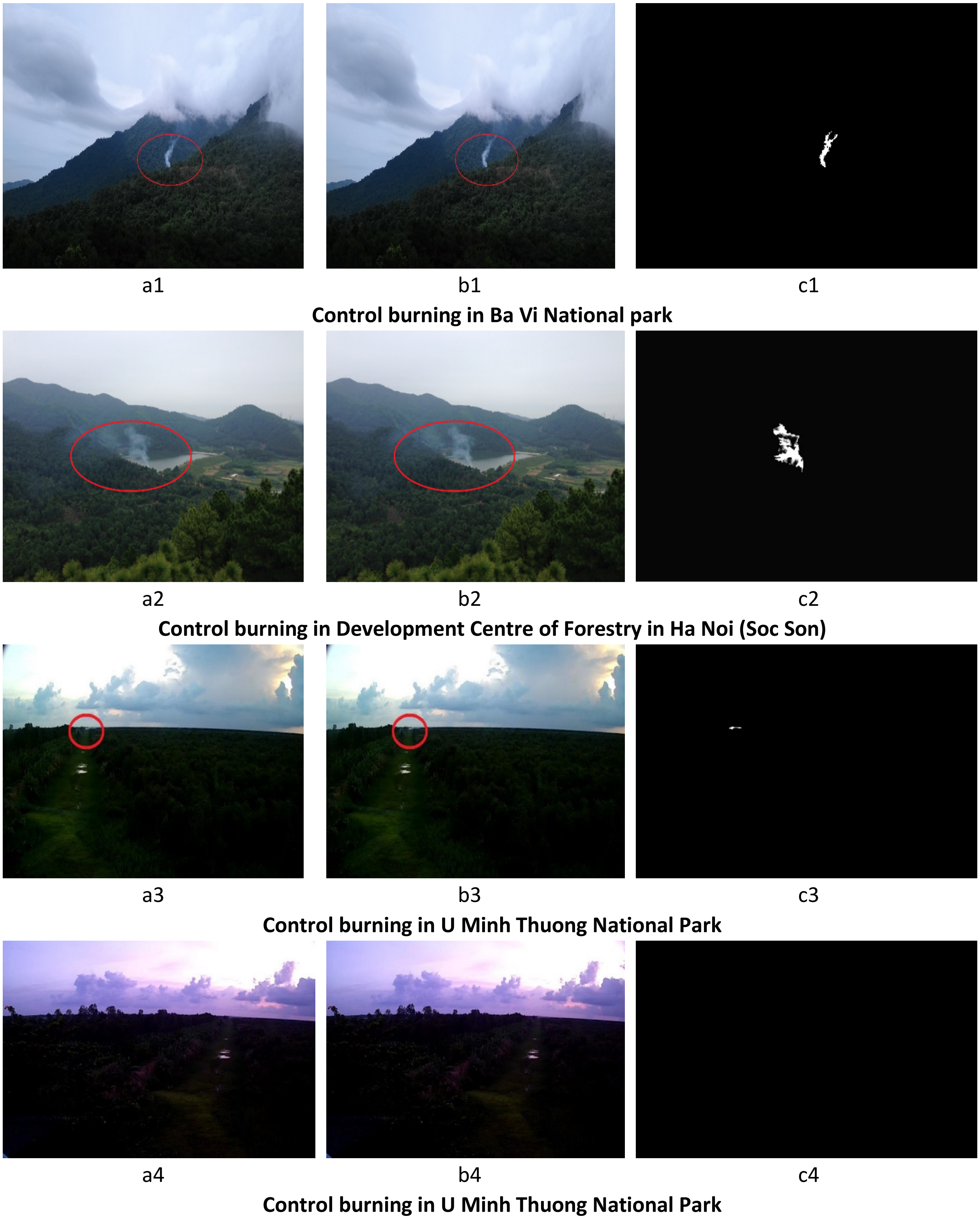

Figure 8. Smoke detection performance; (a_i, b_i) Frame sequences; (c_i) image after processing

- Fire detection results (night time)


a

b

c

Figure 9. Fire detection performance; (a, b) video sequences; (b) image after processing.

Performance results on video sequences show that there are to cases including detected or non-detected. In the second case, smoke or fire cannot be detected because of many different reasons such as the color of background and smoke/fire is the same, and the observation distance from camera effect on the accuracy (fig viii – a4, b4, c4).

4 Conclusions

The Discrete Cosine Transform (DCT) algorithm of each 8 × 8 block is the input for smoke processing and fire detection.

The characteristics of smoke, fire, motion, color and expansion are analyzed directly in the DCT domain to minimize the time and increase the accuracy of the results.

The DCT algorithm used video sequences and control burning, the results show the accuracy of detection up to 97%. The main cause of false detection is the similarity of color between background and smoke, the distance of the camera to the fire location.

The JPEG format processing algorithm from IP Camera can be applied efficiently in early detection of forest fires in Vietnam.

Application software for early detection of forest fires from the ground observation station is designed and developed based on the requirements of forest resource management and minimization of forest fire damage in areas where fire occurs frequently in Vietnam.

The software is integrated with ground observation stations, regular monitoring stations and fire monitoring by IP cameras. The monitoring stations are compact and stable designed with low cost and efficient for forest fire monitoring tasks in Vietnam.

REFERENCES

[1] Chen, T.; Yin, S; Huang, Y.; Ye, Y. The Smoke Detection for Early Fire-Alarming System Based on Video Processing. In *Proceedings of International Conference on Intelligent Information Hiding and Multimedia Signal Processing*, Pasadena, CA, USA, 18-20 December 2006.

[2] Leonardo Millan-Garcia, Gabriel Sanchez-Perez, Mariko Nakano, Karina Toscano-Medina, Hector Perez-Meana and Luis Rojas-Cardenas, *"An Early Fire Detection Algorithm Using IP Cameras"* in Sensors 2012, 12, 5670-5686, pp. 5670-5686.

[3] Schneiderman, R. Trends in Video Surveillance Given DSP an Apps Boost. *IEEE Sign. Process. Mag.* 2010, *6*, 6-12.

[4] Turgay Çelik, Hüseyin Özkaramanlı, and Hasan Demirel, *"Fire and smoke detection without sensors: Image processing based approach"* in 15th European Signal Processing Conference (EUSIPCO 2007), Poznan, Poland, September 3-7, 2007, pp. 1794-1798.

[5] Yuan F. Video-Based Smoke Detection with Histogram Sequence of LBP and LBPV Pyramids. *Fire Safety J.* 2011, *46*, 132-139.

[6] Yu C.; Faon J.; Wang J.; Zhang Y.; State K. Video Fire Smoke Detection Using Motion and Color Features. *Fire Technol.* 2010, *46*, 651-663.